JGR Solid Earth

RESEARCH ARTICLE
10.1029/2019JB018596

Key Points:
- Mean-measured offset records modeled slip only if fault zone width is <5 m, total slip is less than channel spacing, and short time since earthquake
- Postearthquake landscape evolution widens the geomorphic fault zone and smears out initially discrete channel offsets
- Offset measurements have ~30% natural variability, but modeled slip is recovered by taking the mean of multiple offset measurements

Supporting Information:
- Supporting Information S1
- Table S1

Correspondence to:
N. G. Reitman,
nadine.reitman@colorado.edu

Citation:
Reitman, N. G., Mueller, K. J., Tucker, G. E., Gold, R. D., Briggs, R. W., & Barnhart, K. R. (2019). Offset channels may not accurately record strike-slip fault displacement: Evidence from landscape evolution models. *Journal of Geophysical Research: Solid Earth*, *124*, 13,427–13,451. https://doi.org/10.1029/2019JB018596

Received 23 AUG 2019
Accepted 3 DEC 2019
Accepted article online 4 DEC 2019
Published online 23 DEC 2019

Offset Channels May Not Accurately Record Strike-Slip Fault Displacement: Evidence From Landscape Evolution Models

Nadine G. Reitman[1], Karl J. Mueller[1], Gregory E. Tucker[1,2], Ryan D. Gold[3], Richard W. Briggs[3], and Katherine R. Barnhart[1,2]

[1]Department of Geological Sciences, University of Colorado Boulder, Boulder, CO, USA, [2]Cooperative Institute for Research in Environmental Sciences (CIRES), University of Colorado Boulder, Boulder, CO, USA, [3]Geologic Hazards Science Center, U.S. Geological Survey, Golden, CO, USA

Abstract Slip distribution, slip rate, and slip per event for strike-slip faults are commonly determined by correlating offset stream channels—under the assumption that they record seismic slip—but offset channels are formed by the interplay of tectonic and geomorphic processes. To constrain offset channel development under known tectonic and geomorphic conditions, we use numerical landscape evolution simulations along a theoretical strike-slip fault with uniform and steady uplift, erosion, and diffusion. We investigate the influence of four tectonic parameters (fault zone width, earthquake recurrence interval, variance of the recurrence interval, and total slip relative to channel spacing) on offset channel development through multiple earthquake cycles. Analysis of >3,000 automatically measured offsets from >135 simulations suggests ~30% variability in individual measurements, but modeled displacement is recovered by averaging multiple measurements. However, the average of multiple offset measurements systematically underestimates modeled slip except when the fault zone is less than ~5 m wide, total slip is less than channel spacing, and offsets are measured shortly after an earthquake. In these simulations, postearthquake landscape evolution widens the geomorphic expression of the fault zone and modifies apparent channel offsets. We distinguish this "geomorphic fault zone" from the tectonic fault zone (zone of coseismic distributed deformation). This study highlights the capability of landscape evolution models to explore a range of conditions not easily defined in natural examples and the importance of averaging multiple measurements. Our results verify that paleoseismic studies must consider how geomorphic change has modified offset markers and use caution interpreting slip histories with multiple earthquakes.

Plain Language Summary We use landscape evolution simulations to investigate how geomorphic markers (e.g., stream channels) record displacement from earthquakes on strike-slip faults. Stream channels offset across a fault are commonly used to determine the amount of displacement and slip rate of a fault, critical inputs to seismic hazard calculations. For example, Wallace Creek on the San Andreas Fault was famously calculated by Sieh and Jahns (1984, https://doi.org/10.1130/0016-7606(1984)95<883:HAOTSA>2.0.CO;2) to be offset ~128 m in ~3,750 years (~34 mm/year slip rate). However, actual displacement is rarely known, and displaced stream channels are created and modified by both tectonic processes, such as earthquakes, and geomorphic processes, such as erosion. We run landscape evolution simulations to characterize how offset channels develop under certain tectonic and geomorphic conditions. After an earthquake, the initially discrete channel offset is gradually smeared out and diminished. The results imply that offset stream channels accurately record modeled slip only when the zone of faulting is narrow, cumulative slip is less than the distance between stream channels, and offset distances are measured soon after an earthquake. Otherwise, average channel offset distances underestimate modeled slip, which indicates that slip rates and associated seismic hazard may be underestimated on real faults.

1. Introduction

Offset geomorphic markers such as stream channels, ridges, terrace risers, debris flow levees, and alluvial fans are commonly used to estimate lateral displacement along strike-slip faults for recent, historical, and paleoseismic earthquakes (Figure 1a; e.g., Choi et al., 2012, 2018; Frankel, Brantley, et al., 2007; Frankel, Dolan, et al., 2007; Frankel et al., 2011; Gold et al., 2015; Haddon et al., 2016; Klinger et al., 2011; Quigley et al., 2012; Reheis & Sawyer, 1997; Rockwell et al., 2002; Rockwell & Klinger, 2013; Salisbury et al., 2018;

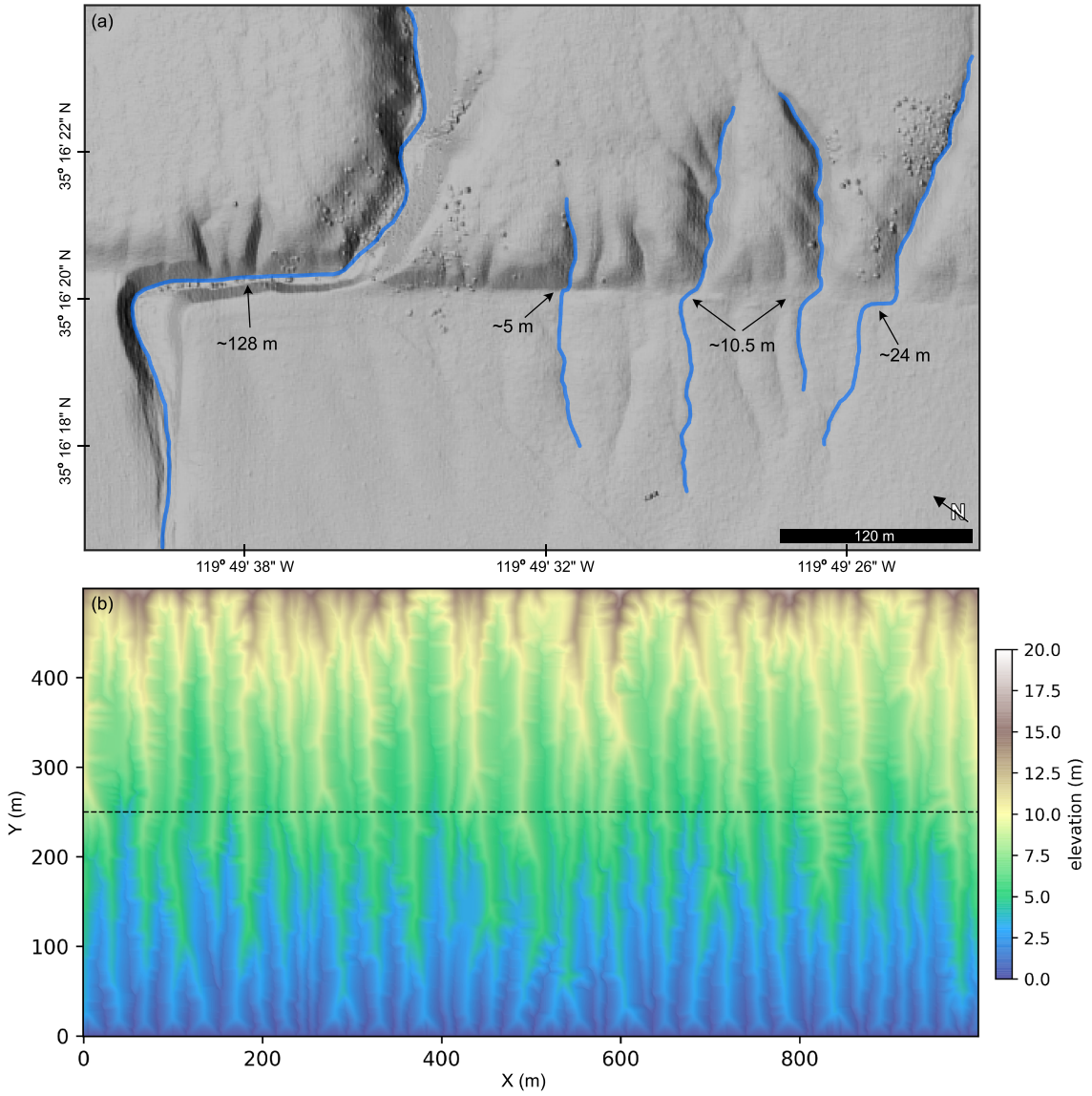

Figure 1. Typical topography along a strike-slip fault. (a) Map view of a portion of the San Andreas Fault at Wallace Creek illustrating single-event (5 m) and multiple-event (≥10 m) offset channels in blue and the natural variability in channel size and spacing. (b) Map view of initial topography prior to faulting for landscape evolution models in this study. This landscape represents an interior portion of a fault segment. The inclined surface forces channels to align (sub)parallel to each other and (sub)perpendicular to the future dextral fault (dashed line), similar to channel alignment in (a). Though channel spacing is more regular in the model domain (~30–35 m) than in the natural world, many small and medium size channels at the Wallace Creek site are similarly spaced (~20-45 m).

Sieh & Jahns, 1984; Wallace, 1968; Zielke et al., 2012, 2015). These measurements are used to determine slip rates, slip distribution along strike, and slip per event to constrain earthquake history and distribution of slip in space and time, critical constraints for seismic hazard calculations. Though these features are used to infer tectonic history, they result from the interplay of tectonic and geomorphic processes, and they degrade in time (e.g., Burbank & Anderson, 2012; Grant Ludwig et al., 2010; Wallace, 1968; Zielke, 2018). The relative importance of tectonic and geomorphic processes in creating observed lateral offsets is actively debated (e.g., Salisbury et al., 2018; Zielke, 2018), and understanding the evolution of offset channels postearthquake is poor compared with normal fault scarps, for which the process of postearthquake erosion and deposition is established (e.g., Burbank & Anderson, 2012). Furthermore, the recent explosion of submeter resolution satellite imagery, lidar, and topographic data sets derived from photogrammetry has created a proliferation of offset marker measurements for recent and historical earthquakes (e.g., Choi et al., 2012, 2018; Fletcher et al., 2014; R. D. Gold et al., 2015; Klinger et al., 2005;

Milliner et al., 2015; Quigley et al., 2012; Rockwell et al., 2002; Rockwell & Klinger, 2013; Salisbury et al., 2012; Zielke et al., 2012), developing better understanding of complex rupture patterns such as fault segmentation, slip variability along strike, and off-fault deformation. Tighter constraints on the processes that create and modify offset channels will help refine slip rates, variation in slip along strike, and distribution of slip in time and may lead to improved understanding of fault interaction and transient changes in fault slip. Such constraints will lead to more informed interpretation of how a population of offset measurements records fault displacement along strike and through time.

A number of factors hinder interpretation of offset markers. The palimpsestic nature of a tectonic landscape complicates interpretation of both individual offset markers from the most recent earthquake and populations of markers in the paleoseismic record by partially concealing or altering older offsets. For example, Sieh (1978) interpreted 9.5-m offsets on the San Andreas Fault in the Carrizo Plain as resulting from the 1857 earthquake, but they were later reinterpreted by Zielke et al. (2010) to be composite offsets resulting from two smaller events. Second, earthquake timing may be lost without suitable deposits and material for precise dating. Though friction and elastic rebound theory predict periodic earthquake recurrence, local factors such as fault segmentation (e.g., DuRoss et al., 2016), pore pressure changes (Amos et al., 2014; Bollinger et al., 2007; Brothers et al., 2011; Ellsworth, 2013; Ge et al., 2009; González et al., 2012; Trugman et al., 2014; Yadav et al., 2016), changes in fluid flow (e.g., Williams et al., 2017), erosional unloading (e.g., Calais et al., 2010; Hampel et al., 2007), and static or dynamic stress changes (e.g., Caskey & Wesnousky, 1997; Hill et al., 1993; Hodgkinson et al., 1996; Kilb et al., 2000; Stein, 1999) can modulate earthquake occurrence and cause transient variations in fault slip. Finally, climate variability may cause differential creation and preservation of lateral offsets because higher incision rates in wet periods are more likely to preserve offsets than aggradational periods that may bury evidence of faulting (e.g., Burbank & Anderson, 2012; Lienkaemper & Strum, 1989; Salisbury et al., 2018).

Perhaps the greatest limitation in developing a deeper understanding of coseismic and interseismic strain release on seismogenic faults is the paucity of data in space and time. Most faults lack detailed records of multiple earthquakes, and some faults have only a few data points at sites measured over tens to hundreds of kilometers of distance along fault length. Statistical analysis suggests at least five earthquake cycles must be measured to accurately estimate slip rate (Styron, 2019). However, earthquake recurrence intervals on major faults range from 10^2 to10^3 years and in some cases exceed 10^4 years (e.g., Koehler & Wesnousky, 2011; Pérouse & Wernicke, 2017; Wesnousky, 2005), whereas a long observation period for geodetic methods is on the order of 2 decades. Paleoseismic trench studies usually investigate up to ~10 ka, spanning 2–10 earthquake cycles depending on the recurrence interval (e.g., compare trenches of Lee et al., 2001 and Scharer et al., 2017), and studies of large populations of offset surface features along strike-slip faults find at most five surface-rupturing paleoseismic earthquakes are preserved in the landscape (e.g., Haddon et al., 2016; Klinger et al., 2011; Zielke, 2018; Zielke et al., 2010, 2012). Displaced geologic units may extend the record back to millions of years, but the history of how that slip accumulated is not preserved (i.e., offset features record total slip, not individual earthquakes). Literature review reveals there are only 10 documented cases of rerupture of a fault segment in the historical record (Schwartz, 2018), and only ~35 sites on ~15 strike-slip faults globally with known earthquake histories that span at least five earthquake cycles (data compiled by Pérouse & Wernicke, 2017, and Yuan et al., 2018). These data deficiencies make it difficult to study the process of offset marker development and modification through multiple earthquake cycles in order to constrain how displaced features record tectonic history and are modified by geomorphic processes.

Numerical model experiments eliminate the normal restrictions of unknown or erratic tectonic history, climate variability, and data availability in the natural world and enable controlled assessment of offset marker evolution through space and time. In this study, landscape evolution models are used to simulate lateral faulting with a predefined tectonic history and observe erosional processes that occur over 10^2–10^4 years to isolate the influence of tectonic parameters on the fault zone landscape and offset marker development. Unlike in the natural world, the earthquake history and slip distribution are known and can be compared to measured offsets in a quantitative error analysis. We determine under which tectonic conditions offset channels faithfully record single-earthquake and cumulative fault slip, constrain the natural variability of a population of offset measurements from a single earthquake on a single fault segment, and infer how to interpret large populations of offset measurements for recent and paleoseismic earthquakes.

2. Methods

2.1. Landscape Evolution Model Setup

The landscape evolution model follows the models of Duvall and Tucker (2015) and Gray et al. (2018). Landscape evolution and strike-slip displacement are based on the following equation:

$$\frac{\partial z}{\partial t} = U - V(y)\frac{\partial z}{\partial x} - \left(KA^{1/2}S - E_{crit}\right) + D\nabla^2 z, \quad (1)$$

where z is height of the landscape (m), t is time (year), x is fault-parallel direction (m), y is fault-perpendicular direction (m), U is relative rock uplift (m/yr), $V(y)$ is time-averaged lateral displacement rate (m/year), K is erodibility (year^{-1}), A is drainage area (m^2), S is slope gradient (positive downward), E_{crit} is a threshold on stream power (m^2/year), and D is hillslope diffusivity coefficient (m^2/year). The reader is referred to Duvall and Tucker (2015) for full definition and nondimensionalization of the landscape evolution model. The only modification is in the lateral displacement term because in Duvall and Tucker (2015) displacement across the fault ($V(y)$) was represented by a step function. To more accurately represent surface displacement observations across strike-slip faults (e.g., Binet & Bollinger, 2005; Delong et al., 2016; Gold et al., 2015; Massonnet et al., 1993; Milliner et al., 2015; Okada, 1985; Savage & Burford, 1973; Wang et al., 2014), we represent the displacement field with

$$d(y) = \frac{d_0}{2}\tanh\left(-\frac{y - y_0}{y_*}\right), \quad (2)$$

where d_0 is displacement per earthquake (m); $y - y_0$ is distance from the main fault (m); y_0 is location of the main fault (m); and y_* is fault zone width (m), the length scale that displacement decays away from the fault when fault zone width is >0. Average displacement rate, $V(y)$, is $d(y)$ divided by the recurrence interval.

The model is initialized with a channelized landscape such that (sub)parallel channels and ridges align (sub) perpendicular to a strike-slip fault that crosses the center of the model domain (Figure 1b). The model domain simulates a middle section of a longer strike-slip fault or fault section to avoid fault-tip effects. The initial topography approximates a simple setting for a typical strike-slip fault, but with sufficient channels to make multiple offset measurements and perform statistical analysis for each model. The initial condition topography was created by evolving a smooth inclined plane with millimeter-size randomness to steady state before strike-slip faulting begins using the model described in equation (1) with $V(y) = 0$ and all other parameter values the same as in model runs. Model time begins when strike-slip faulting begins. Initial channel spacing at model time 0 is ~35 m, which results from the angle of the inclined plane evolved to steady state. The grid pixel size is 1 m^2, and the model domain is 1,000 m in the x direction and 500 m in the y direction.

We used the open-source landscape evolution toolkit Landlab (Hobley et al., 2017) to route flow across the landscape and handle stream incision and hillslope diffusion on a 2-D grid under uniform and steady uplift, erosion, and diffusion conditions. Models are run for 10 ka with a 1-year time step. Incision and diffusion parameters are held constant throughout all model runs. We use $D = 0.01$ m^2/year and $K = 0.003$ year^{-1} for diffusion and erodibility, a threshold on stream power of 5×10^5 m^2/year, and a background uplift rate of 0.001 m/year to maintain gradient across the model domain. The values of the geomorphic process parameters were chosen to simulate an alluvial semiarid environment, similar to southern California, but the model is not tuned to a particular location or climate.

The numerical model is a simple representation of faulting and landscape evolution. Simplicity is an asset because it keeps the parameter space smaller and the results easier to understand and interpret. However, there are some potentially important effects of the natural world that are not included. A more realistic depiction of geomorphic processes could include flow routing that allows for spreading or narrowing of flow in response to topography (Tarboton, 1997), deposition by surface flow (Shobe et al., 2017), lateral channel migration (Langston & Tucker, 2018), and the action of storm events and debris flows. Though the model does not explicitly include depositional processes, diffusion is sufficient for valleys to fill in when cut off from main drainages. Furthermore, characteristics of the initial topography (e.g., surface roughness, distribution of channel sizes, material strength, gradient, and variations in gradient) may play important roles in how

offsets are recorded in a landscape. Though beyond the scope of this study, the relationship between characteristics of the geomorphic surface and offset preservation warrants further investigation.

Recent studies use landscape evolution modeling to explore geomorphic response to lateral offset at varying slip rates along strike-slip faults. Duvall and Tucker (2015) modeled long-term, (10^4–10^6 years), catchment-wide response to lateral faulting and found that ridges perpendicular to the fault migrate with fault displacement for slow slip rates. Gray et al. (2018) demonstrated that deflected drainage orientation may be controlled by lateral displacement rate in the Mecca Hills of California, and Harbert et al. (2018) found that channel offset distance correlates to shutter ridge length for creeping faults with 1–10 mm/year slip rates and >250-m displacement over 75–750 ka. The main differences between this study and previous work are tectonic, geographic, and temporal scope, and analysis of model outcome. We focus on individual channels in the fault zone region, over 2–15 earthquake cycles up to 10 ka, and up to 30- to 200-m total slip. The other primary difference is in consideration and interpretation of model results. We evaluate model output by measuring apparent channel offset distances as in paleoseismic studies, which relates the results of landscape evolution modeling directly to earthquake geology studies of active faults on timescales relevant to earthquake hazards analysis.

2.2. Tectonic Parameters

We investigate four characteristics of deformation and earthquake history along active faults to evaluate if and how tectonic parameters are preserved in fault-zone geomorphology and affect the evolution and preservation of offset channels. The parameters tested are fault zone width (FZW), earthquake recurrence interval, coefficient of variation of the recurrence interval (CV_{time}), and total slip (Figure 2). In the following sections we describe the details of the experimental design as well as the geologic questions addressed with each experiment.

Each tectonic parameter was explored using a parameter study relative to a base case scenario in which all other parameters remain constant (i.e., one parameter is tested in each model set). Base case parameters are deliberately simple so that the resulting signal can be attributed to the tectonic characteristic explored in that model set. Base case model parameters are 0-m fault zone width, 666-year recurrence interval, periodic earthquake recurrence ($CV_{time} = 0$), and 30-m total slip distributed in 15 earthquakes with 2-m slip per event (3 mm/year slip rate). We use 0-m fault zone width for the base case because modeled slip is recoverable in both manual and automatic measurements, as discussed in section 2.3.1. All models run for 10 ka. Parameters for all model runs are in Table S1 in the supporting information, and model code and configuration files are available in an online repository (Reitman et al., 2019).

2.2.1. Fault Zone Width

Fault zone width (FZW) is here defined as the zone of coseismic distributed deformation extending orthogonal from the primary fault trace. In 44 model runs, we test values from 0 m, in which all deformation occurs on the primary fault, to 500 m, in which deformation is spread throughout the model domain in the *y* direction according to equation (2) (Figure 2a).

2.2.2. Earthquake Recurrence Interval

The earthquake recurrence model set tests the amount of time between periodic ($CV_{time} = 0$) earthquakes of equal size. Slip per event and recurrence interval covary because total slip (30 m) is constant for this model suite. In 39 model runs, we test values from a 1-year recurrence interval with 0.003-m slip per event to a 5,000-year recurrence interval with 15-m slip per event (Figure 2b). This model set simulates and compares small, frequent earthquakes (akin to creep) versus infrequent, large earthquakes.

2.2.3. Variance of Recurrence Interval

Coefficient of variance of the recurrence interval (variability of time between earthquakes, CV_{time}) tests the difference between periodic, semiperiodic, random, and clustered earthquake histories. CV_{time} is the standard deviation of recurrence interval divided by the mean recurrence interval. CV_{time} of 0 is perfectly periodic; $0 < CV_{time} < 1$ is semiperiodic; $CV_{time} = 1$ is random; and $CV_{time} > 1$ is clustered. Analysis of CV_{time} of global strike-slip faults shows a range of CV_{time} from 0.1 to 1.2 (Kagan & Jackson, 1991; Sykes & Menke, 2006; Yuan et al., 2018). In 42 model runs, we test earthquake histories with CV_{time} from 0 to 1.3 (Figures 2d–2f). Earthquake intervals are determined by selecting at random from normal distributions with increasing standard deviations centered around regularly spaced intervals. The standard deviation of the normal distribution is prescribed, and CV_{time} of the resulting earthquake history is calculated. Each

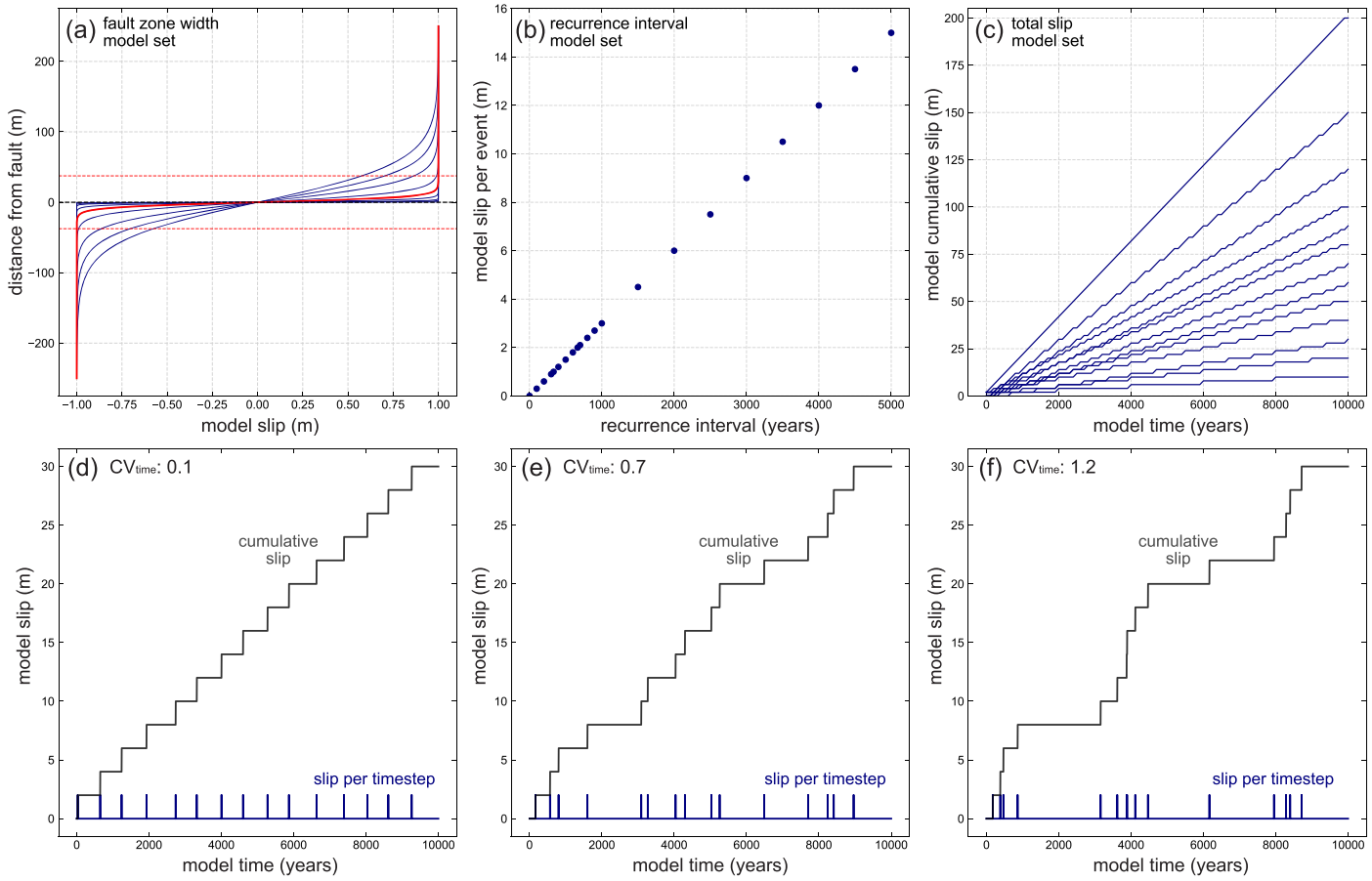

Figure 2. Tectonic parameters investigated in sets of model runs. One parameter value changes incrementally in each model run. (a) Set of model runs testing varying fault zone widths (FZW). Curves show how displacement is distributed in the fault zone for example FZWs of 0–400 m for earthquakes with 2-m slip. Red line is 50-m FZW, and red dashed lines show where offsets are automatically measured when FZW is 50 m. (b) Set of model runs testing varying earthquake recurrence intervals. Recurrence time and slip per event covary because total slip is constant in this model set. (c) Set of model runs testing varying total slip relative to channel spacing. (d–f) Example model runs from the model set testing varying coefficient of variation of the recurrence interval (CV_{time}) representing (d) nearly periodic ($CV_{time} = 0.1$), (e) semiperiodic ($CV_{time} = 0.7$), and (f) clustered ($CV_{time} = 1.2$) earthquake histories.

model run has 15 earthquakes with 2-m slip per event. Slip per event is held constant because we can only vary one parameter at a time; otherwise, we would not be able to discern the cause of any resulting signal.

2.2.4. Total Slip

The total slip model set tests how channel spacing relative to total slip affects how offset channels record cumulative slip. In 13 model runs, we test values of total slip from 10–200 m (slip rates of 1–20 mm/year; Figure 2c). The initial landscape has ~30 channels spaced ~35 m apart across the 1,000-m model space (Figure 1b). The ratio of total slip to channel spacing for the base case model is 0.86 (30-m total slip/35-m channel spacing) and ranges from 0.29 to 5.7 for all model runs.

2.3. Analysis of Model Output

2.3.1. Automatic Offset Measurements

Model output is evaluated by measuring offset channel distances with an algorithm (Reitman et al., 2019) that identifies and locates offset channels and calculates offset distance. The algorithm is based on drainage area, connected channel systems, and direction of faulting (Figure 3). Drainage area is calculated from the model topography (Figure 3a) using the Landlab FlowDirectorD8 and FlowAccumulator components (Hobley et al., 2017), and channels are identified with a threshold drainage area. The selected channels are analyzed with a connected components algorithm (Van der Walt et al., 2014) to map connected channel systems across the fault (Figure 3b). Thalweg locations are automatically identified where channels intersect profiles on both sides of the fault. Thalweg locations are matched (Figure 3c) by relative location, direction of

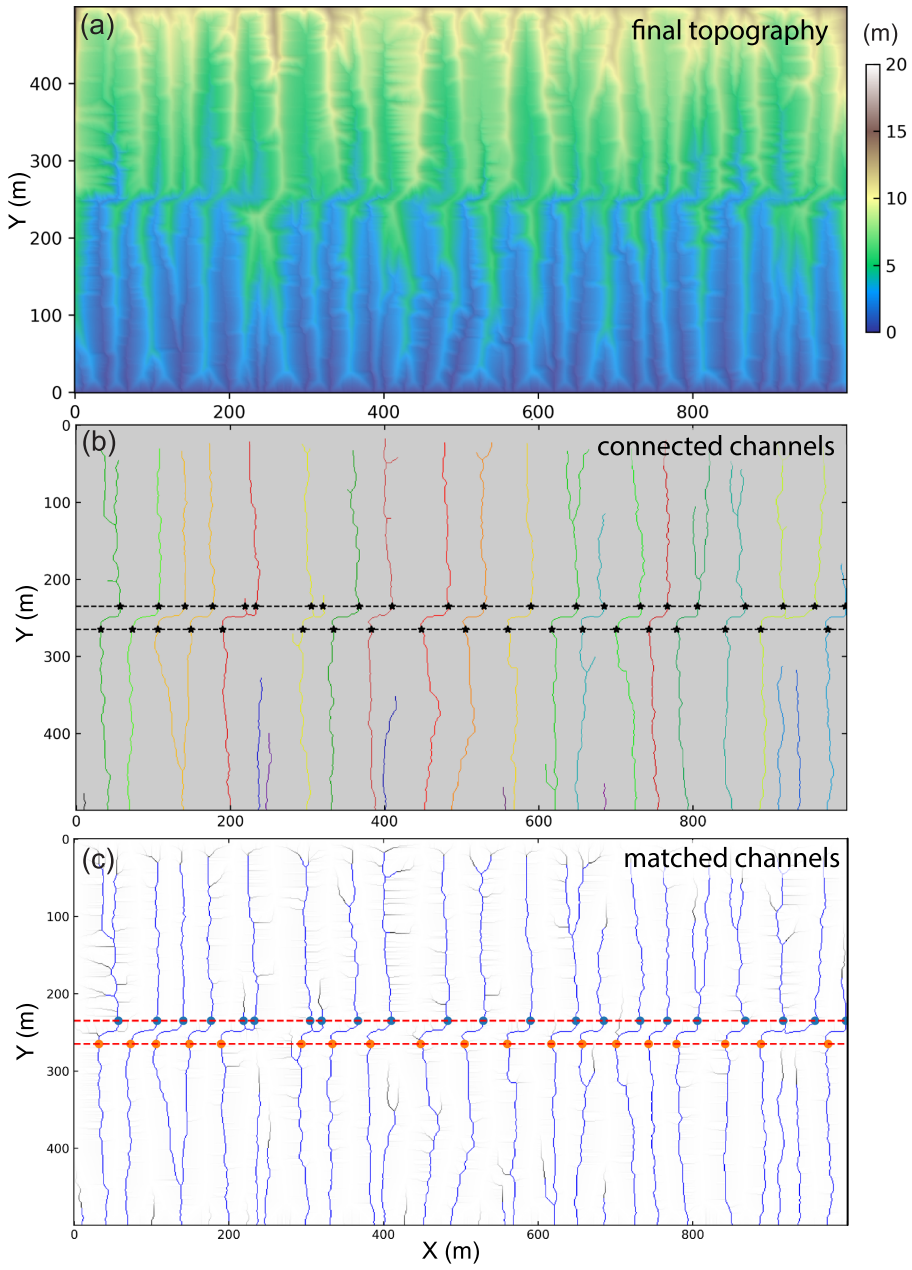

Figure 3. Automatic offset measurement method. (a) Map view of final topography from the base case model run with 0-m fault zone width, periodic earthquakes and 30-m total slip. Color is elevation. (b) Thalweg locations (black stars) identified on both sides of the fault where connected channels (solid colored lines) intersect profile lines (dashed lines) located ±10 m from the fault trace. (c) Thalwegs (blue and orange circles) correlated across the fault. Offset distance is distance between correlated thalwegs. Blue lines are channels with drainage area ≥1,000 m^2. The ratio of cumulative displacement to channel spacing is ~0.75 for this time step.

faulting (dextral or sinistral), and rules, in part based on the connectedness of channel systems, to deal with some complex situations such as beheaded and captured channels. The user sets the threshold drainage area (10^3 m^2 in this study), distance of the profiles on either side of the fault, and direction of faulting (dextral in this study). To ensure that the measurements are taken sufficiently outside of the fault zone, measurement distance in this study is ±10 m orthogonal to the fault (20-m total) when FZW is ≤10 m, and ±0.75*FZW (total of 1.5*FZW) when FZW is >10 m (Figure 2a). Offset distances are then identified and measured automatically without any further user input. The algorithm was designed to work with output from

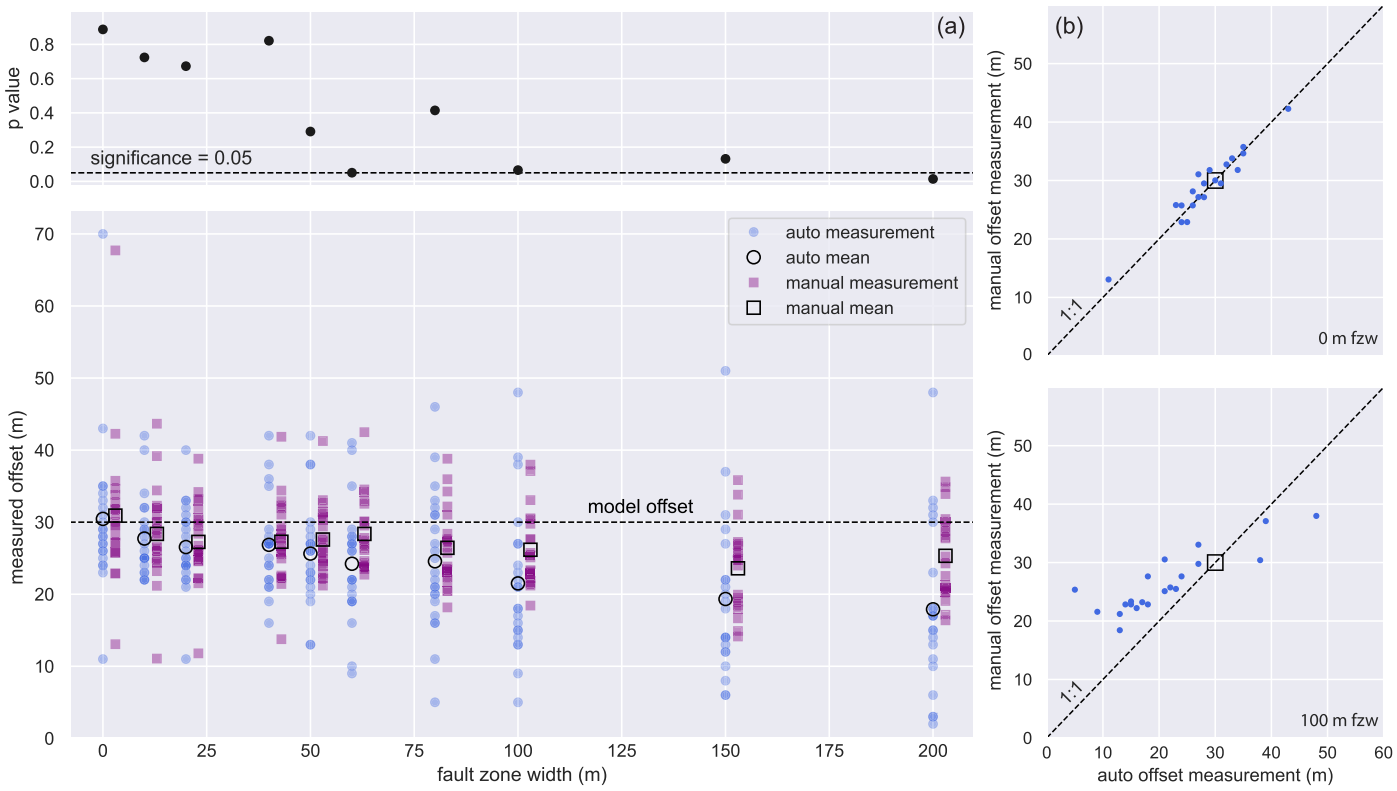

Figure 4. Comparison of manual and automatic offset measurements. (a) Automatic (blue circles) and manual (purple squares) measurements for 10 models with different fault zone widths (FZW). *P* values from *t* test comparing manual to automatic measurements for each FZW are shown in the top panel. (b) Automatic versus manual measurements (dots) for models with 0-m (top panel) and 100m (bottom panel) FZW. Open square is modeled slip.

these numerical models. Though it can be implemented in more complex scenarios, channels must be oriented nearly perpendicular to the fault for the code to work properly because channel obliquity relative to the fault zone is not tested in these models.

To validate output from the code, we compared channel offsets measured manually to those measured automatically on 10 models with different fault zone widths (Figure 4). The manual measurements were done by projecting linear average thalweg locations into the fault (e.g., Gold et al., 2015) and were performed blindly in that the user did not know the magnitude of individual offsets as they were measured. Automatic and manual measurements are statistically indistinguishable both in terms of magnitude and variance when fault zone width is less than 50 m (Figure 4a). However, when fault zone width exceeds 50 m, automatic measurements exhibit greater variance than manual measurements, and the mean of automatically measured offsets is systematically lower than the mean of manually measured offsets. Although only the 200-m FZW data are significantly different (*t* test, $p = 0.014$; Figure 4), the 60-m and 100-m FZW data have a *p* values close to the significance level of 0.05.

We believe that some of the bias when fault zone width is greater than 50 m may be due to the aperture of the automatic measurements; however, increasing the measurement aperture did not improve results because of the natural variability in thalweg locations at greater distances from the fault. In this case, projecting average thalweg locations into the fault (as a human does) may be more accurate than taking single-point locations of thalwegs (as the automatic method does). Therefore, though we present results up to 300-m fault zone width for completeness (Figures 5a and 5b), further discussion considers only results when fault zone width is less than 50 m because we have validated the automatic method for fault zones less than 50 m wide.

The primary limitations of the automatic measurement algorithm are (1) the use of point source measurements (i.e., matching thalwegs), as opposed to matching cross profiles of channel shape (e.g., Zielke & Arrowsmith, 2012) or linear projections of average thalweg location (e.g., Gold et al., 2015) and (2) the

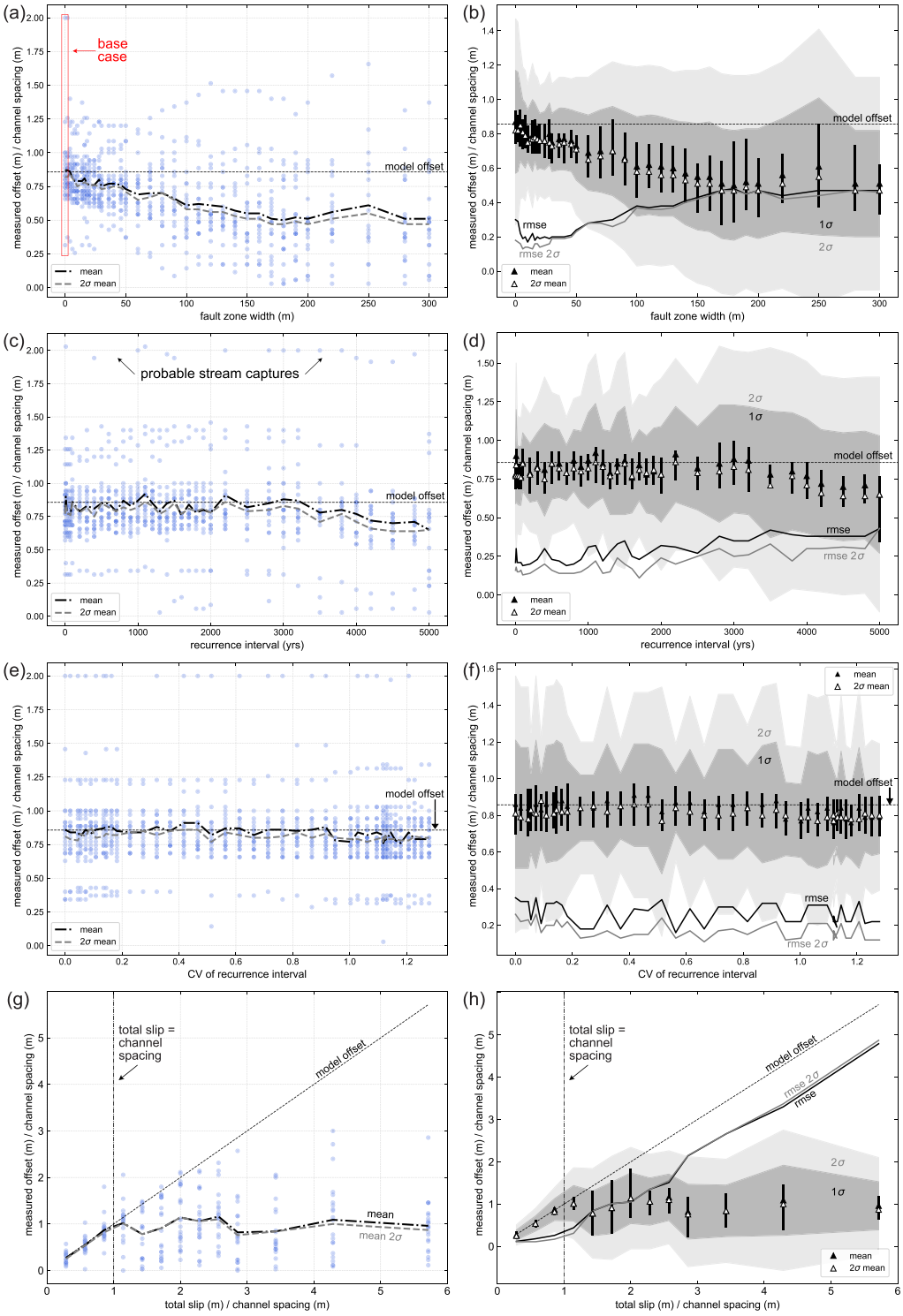

Figure 5. Offset distances automatically measured at the end of each model run for (a and b) fault zone width, (c and d) earthquake recurrence interval, (e and f) variance of the recurrence interval, and (g and h) total slip model sets. Left side panels (a, c, e, and g) show all offset measurements (blue circles) with measured mean offset (black dash-dot line), measured mean offset excluding measurements >2σ (gray dashed line), and modeled slip (black dashed line). Right side panels (b, d, f, and h) show interquartile range (black bars), measured mean (black triangles), measured 2σ mean (white triangles), 1σ standard deviation (dark gray shading), 2σ standard deviations (light gray shading), root mean square error (RMSE) (black solid line), 2σ RMSE (gray solid line), and modeled slip (black dashed line).

lack of uncertainty estimate. Despite these limitations, a major advantage of our automated thalweg matching approach is its computational efficiency. We use the algorithm to measure a total of ~60,000 offset measurements. This analysis would not be possible for a human using tools such as LaDiCaoz (Zielke & Arrowsmith, 2012). Furthermore, we propose that matching thalwegs is a sufficient approach for these numerical models because the location of the thalweg is not nebulous as it may be in the natural world. In our numerical models, all flow from each pixel is routed into one pixel, so instead of building wide channels with flat bottoms and migrating thalwegs within those channel margins, channels incise deeper and become entrenched (Kwang & Parker, 2019). Thus, thalweg locations in the models do not migrate as much as they might in the real world, and the exact location of the thalweg is certain.

Instead, a potentially greater source of uncertainty is related to where the measurement is taken relative to the fault (i.e., farther upstream or downstream). However, this type of measurement uncertainty exists in correlating channel cross profiles, too, as the user must choose the profile's distance from the fault (Zielke & Arrowsmith, 2012). To address this issue, we estimate an uncertainty of ±2 m (2*pixel dimension) when we compare model offsets to offsets measured on real faults because the exact location of the thalweg in the models is known but may shift by a few pixels if the measurement is taken either upstream or downstream. In summary, we think that the algorithm's accuracy is sufficient for analysis of our model output—an assumption corroborated by the nearly identical human and automatic measurements for narrow fault zones (i.e., <50 m; Figure 4)—and it makes this investigation possible.

2.3.2. Aspect Ratio of Fault Zone Topography (Ar)

Aspect ratio, Ar, measures the ratio of topography in the fault zone that is oriented fault parallel versus fault perpendicular. Topography that is oriented fault perpendicular has pixels with fault-parallel aspects (45–135° and 225–315° for a fault with 90° strike), and topography-oriented fault parallel has pixels with fault-perpendicular aspects (315–45° and 135–225° for a fault with 90° strike). Higher values of Ar indicate more topography is aligned fault parallel (and has an aspect between 315–45° and 135–225° in this model setup). The utility of the Ar metric was first demonstrated in the work of Gray et al. (2018), in which variation in Ar corresponded to the amount of basin reorganization due to lateral displacement and off-fault deformation. Our landscape evolution model is constructed such that channels and ridges start with an approximately fault-perpendicular orientation prior to faulting. As lateral displacement accumulates through time, topography near the fault reorganizes toward a more fault-parallel orientation, increasing the value of Ar around the fault zone.

3. Results

3.1. Tectonic Parameters

Measured channel offset distances from all model runs are shown in Figure 5. Apparent offset distances were measured automatically on topography output from the final time step of each model run. We calculate results from each model run for total means and means with offset measurements greater than two standard deviations (σ) from the measured mean excluded (2σ-mean), in order to account for offset measurements that geologists might consider outliers. All mean values are reported in Table S1. We use the mean to account for uncertainty in individual measurements. Offset channel measurements are presented in nondimensional form relative to channel spacing. Normalizing against channel spacing makes stream captures more obvious as they are often approximately double channel spacing (i.e., apparent offset/channel spacing ≈2). For the base case model (with 0-m fault zone width, no open interval, and periodic earthquakes), the mean of all offset measurements accurately records modeled cumulative displacement, verifying that both the offset channels and offset measurements record imposed displacement in a simple situation.

3.1.1. Fault Zone Width

When FZW is small, mean and 2σ-mean channel offset measurements record cumulative modeled slip, but they increasingly underestimate modeled slip as FZW increases (Figures 5a and 5b). These models have 30-m total slip and no open interval (time between last earthquake and time of measurement) at the end of the model run. For models with narrow fault zone width (0–4 m), mean measured offset distances are within 10% of modeled slip (Figure 5a). Nearly 75% of automatic offset measurements underestimate modeled slip when FZW > ~50 m, so further discussion excludes these model runs. Similar to the automatic measurements, manually measured mean offset distance underestimates modeled slip for all models except for 0-m FZW (Figure 4a).

3.1.2. Earthquake Recurrence Interval

For most recurrence intervals, mean and 2σ-mean channel offset measurements slightly underestimate cumulative modeled slip (Figures 5c and 5d). Open interval for these models varies, but is generally short, and is 0 years for the model with a 666-year recurrence interval. Mean measured offset distances are similar for earthquake recurrence intervals of 0–3,000 years and mostly are within 10% of modeled slip. For models with recurrence intervals of 3,500–5,000 years, mean measured offset distances underestimate modeled slip by ~15–30%. Standard deviation and RMSE both increase slightly for recurrence intervals >2,500 years (Figure 5d).

3.1.3. Variance of Recurrence Interval

Mean and 2σ-mean measured offset distances are within 10% of cumulative modeled slip for all models, but models with random and clustered recurrence intervals ($CV_{time} \geq 1.0$) have means that tend to slightly underestimate modeled slip. Open interval for these models varies, but tends to be long, and is 676 years for the model with $CV_{time} = 0$. RMSE and standard deviation are similarly constant, varying slightly without a consistent trend (Figure 5f).

3.1.4. Total Slip

In models with total slip less than channel spacing (total slip/channel spacing < 1), mean and 2σ-mean measured offset distances record cumulative modeled slip, but they underestimate cumulative modeled slip in models with total slip greater than channel spacing (total slip/channel spacing > 1; Figures 5g and 5h). These models do not have an open interval at the end of model run time. RMSE increases nearly linearly as total slip increases. Standard deviation increases as total slip increases until total slip is equal to channel spacing and then is mostly steady for models with total slip greater than channel spacing (Figure 5h).

3.2. Variance of Measured Offsets

Individual channel offset measurements range widely for all models (Figures 5 and S5). We describe variability in measured offsets using the coefficient of variance of all the offset measurements from one model run ($CV_{slip\text{-}spatial}$), calculated as σ divided by the mean of measured offsets. For models in the FZW model set with FZW ≤50 m and models in the CV_{time} model set with CV_{time} <1.0, average $CV_{slip\text{-}spatial}$ is 0.29. Two model runs have 0-m FZW and no open interval at the end of the model run (first models in Figures 5a–5d). Considering only these models, the total range in offset measurements is 36–233% of modeled slip or 31–200% of channel spacing. These two models have $CV_{slip\text{-}spatial}$ of 0.34. Although the mean measured offset in these two models approximately records modeled slip (101% of modeled slip), it is skewed by a large apparent offset of double channel spacing that results from a stream capture. Most geologists would recognize this large offset of more than double imposed slip as a stream capture and exclude it, but sometimes, stream captures are not obvious due to postearthquake erosion and deposition. Therefore, we calculate and report both $CV_{slip\text{-}spatial}$ and $2\sigma\text{-}CV_{slip\text{-}spatial}$, when offset measurements >2σ from the measured mean are excluded. See Table S1 for all $CV_{slip\text{-}spatial}$ calculations. For these two models, when outliers are excluded, measured 2σ-mean value is within 5% of modeled slip but slightly underestimates modeled slip, and $2\sigma\text{-}CV_{slip\text{-}spatial}$ is 0.21.

3.3. Offset Analysis Through Multiple Earthquake Cycles

We analyzed 28 models throughout model run time (10 ka, 15 earthquake cycles), with offset distances measured every 100 years. Typical patterns are illustrated by three models (with recurrence interval of 250, 666, and 2,000 years and all with 0-m FZW) shown in Figure 6. First, for all models with total slip greater than channel spacing, mean measured offset distance approximately tracks modeled slip while total slip is less than channel spacing (Figure 6a, model time 0–4 ka) and then underestimates modeled slip as total slip exceeds channel spacing (Figure 6a, model time 4–10 ka). This is illustrated by the increase in small offsets around 6 ka model time when existing channels are captured by other drainages. This pattern is similar to the observations of offset distances measured on final topography from the total slip model set (Figures 5g and 5h). Second, comparing Figures 6b and 6c illustrates that the variance in measured offset distances (standard deviation in gray shading) does not increase with increased total slip for models with short recurrence intervals (<1 ka, Figure 6b) but does increase for models with longer recurrence intervals (greater than ~1 ka, Figure 6c).

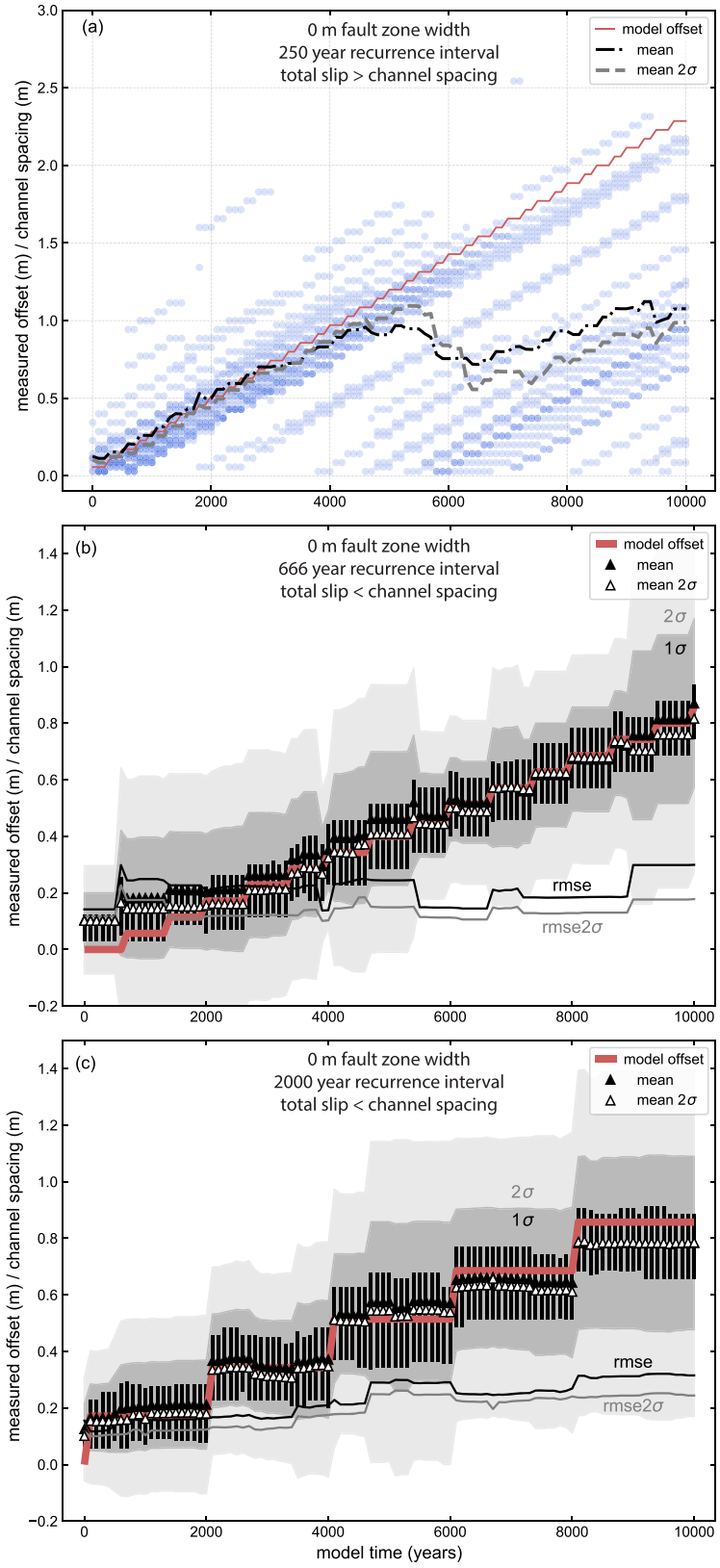

Figure 6. Offset distances measured every 100 years throughout model time for three example model runs. (a) Offset measurements (blue dots) for the model with 80-m total slip. (b) Base case model with a 666-year recurrence interval and (c) the model with a 2,000-year recurrence interval with standard deviations, means, root mean square error (RMSE), and interquartile range (black bars).

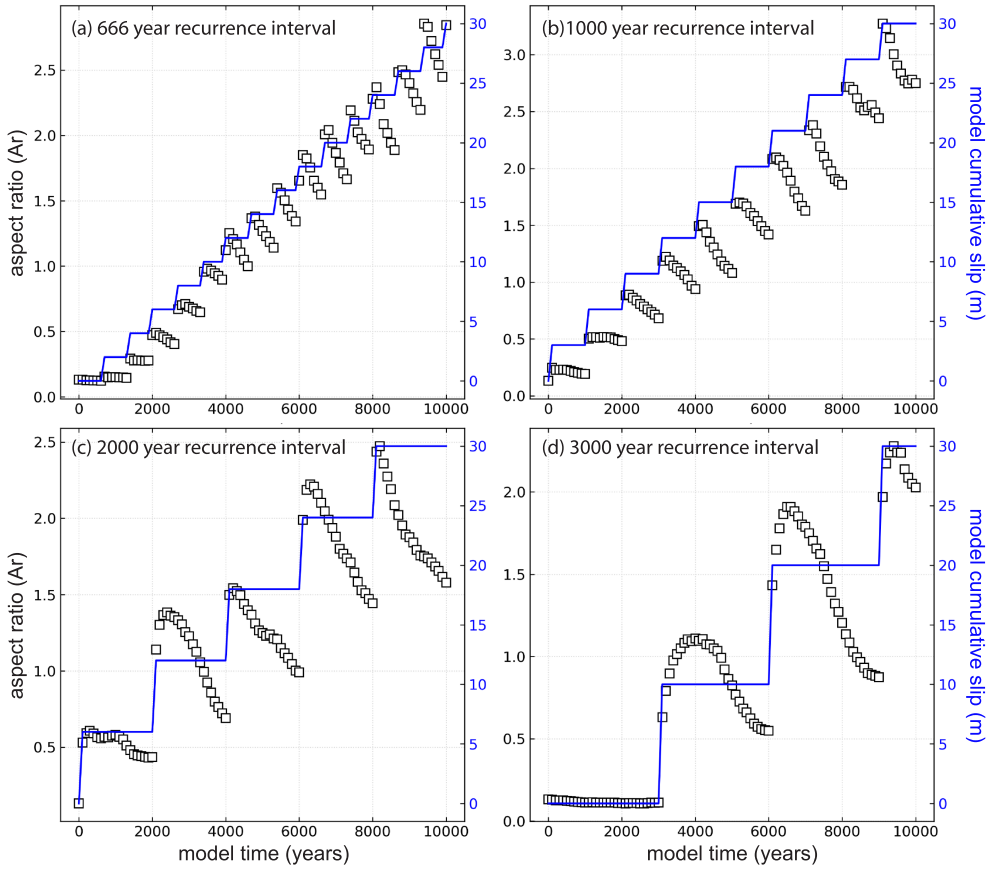

Figure 7. Evolution of fault zone topography aspect ratio (Ar) throughout model time for models with recurrence intervals of (a) 666 years, (b) 1,000 years, (c) 2,000 years, and (d) 3,000 years. Ar is the ratio of fault-parallel topography to fault-perpendicular topography within 20 m of the fault. Higher values of Ar indicate that more topography is aligned fault-parallel or subparallel. Squares are Ar measured every 100 years. Blue line is cumulative model slip. Models shown have 0-m fault zone width, periodic earthquakes, and 30-m total slip.

3.4. Orientation of Fault Zone Topography

Ar is a measure of what fraction of fault zone topography is oriented parallel to the fault, and it is sensitive to multiple tectonic parameters. Ar increases with cumulative slip and thus cannot be used to compare models with variable total slip. Additionally, Ar is sensitive to the area over which it is measured because it is a ratio and thus is meaningless in comparing models with different fault zone widths. Ar also correlates with time since the last earthquake, so models with variable open intervals (recurrence interval and CV_{time} models) cannot be quantitatively compared with Ar either. Therefore, we use Ar to examine the evolution of fault zone topography through model time within individual model runs (Figure 7).

Evolution of Ar for models with 666- to 3,000-year recurrence intervals is shown compared to cumulative slip in Figure 7. Ar is mostly stable and decreases slightly in time in the absence of lateral displacement, an indication that fault zone topography is becoming more fault perpendicular (see Years 0–3,000 of Figure 7d). This is expected behavior because the model is designed so that channels initially align fault perpendicular. Once lateral displacement begins, Ar is positively correlated with cumulative slip, and there are discrete increases in Ar with each earthquake (Figure 7). The increase in Ar as lateral displacement accumulates indicates that fault zone topography evolves to be more fault parallel with greater displacement; however, the increase is not linear. After each earthquake, Ar continues increasing for 100–1,000 years and then decreases until the next earthquake (Figures 7c and 7d). The size and timing of the increase and decrease in Ar correlate with the size of the displacement. In most cases, Ar decreases to a level less than or equal to the value immediately following the last earthquake.

This pattern suggests that fault zone topography responds to each earthquake with a pulse of fault zone modification, and the timescale of the reorganization process correlates with the magnitude of displacement. Though not investigated in this study, the postearthquake landscape response and evolution of fault zone topography are likely modulated by lithology and climate of the fault zone. The evolution of Ar, observations of channel morphology between earthquakes, and variability in apparent channel offset distances lead us to propose the concept of the geomorphic fault zone (explored in detail in section 4.3), which is distinct from the tectonic fault zone, or zone of coseismic distributed deformation (FZW in this study).

4. Discussion

Analysis of this set of well-controlled numerical experiments of how a strike-slip fault zone and offset markers respond to varying tectonic conditions enables us to better constrain what we can and cannot expect to infer from displaced channels and fault zone geomorphology in the natural world. Unless otherwise stated, all discussion is based on results of all data (i.e., including offset measurements $>2\sigma$).

4.1. Influence of Tectonic Parameters

We find that fault zone width and total slip relative to channel spacing modulate channel offset development and preservation, but earthquake recurrence interval and variance of the recurrence interval mostly do not (Figures 4–6). From Figure 5 it is evident that mean of measured offsets is similar to modeled cumulative slip only when fault zone width is <~5 m, recurrence interval is ≤3,000 years, CV_{time} is ≤~0.9, and cumulative slip is less than channel spacing.

Mean measured offset captures modeled cumulative slip only when fault zone width is extremely narrow (i.e., less than ~5 m) and underestimates modeled slip for all wider fault zones (up to 50 m) by both manual and automatic measurement methods (Figures 4a, 5a, and 5b). We think this is due to two primary factors. First, the large width of a zone of distributed deformation compounded by the meandering nature of channels makes it difficult to choose a location that provides an accurate measure of channel displacement. Increasing the measurement aperture did not improve results because of the natural variability in thalweg locations at greater distances from the fault. Second, wide fault zones have more area for an offset in a channel to be modified by geomorphic processes postearthquake. Thus, wider fault zones less faithfully record modeled displacement. Furthermore, we do not test the effects of channel obliquity to the fault, and channels with different flow orientations with respect to the fault may not share this underestimation bias or may have an overestimation bias.

Second, we observe that maximum recorded offset distance is limited by channel spacing and channels do not record slip greater than channel spacing (Figures 5g, 5h, and 6a). We suggest this occurs because downstream portions of channels are likely to disconnect from their original upstream portion (head) and reconnect to or capture a different head, obscuring original offset distances. A similar observation is described by Walker and Allen (2012), who found that most rivers along the Kuh Banan fault in Iran are offset less than 100 m, despite total fault displacement of 5–7 km. Walker and Allen (2012) suggest that shutter ridges control large offset distances by protecting the surrounding landscape so that the river is inhibited from cutting a new channel or being captured until the shutter ridge has been displaced beyond the river head. Similarly, Harbert et al. (2018) found that channel offset distance correlates with shutter ridge length in numerical models and in the Marlborough fault system in New Zealand. In a recent study at the Van Matre Ranch site, Salisbury et al. (2018) upended long-standing interpretations of beheaded channels supposedly representing small offsets along the San Andreas Fault. They found that the sediments in the channels were too old to correlate to small drainages nearby, as had been previously thought, and instead must be correlated to other drainages that had been faulted farther away. This example illustrates some of the complications that occur when cumulative slip exceeds channel spacing, even when beheaded channels are not reoccupied. Thus, our work confirms that total fault slip is not recorded by offset channels when cumulative slip exceeds channel spacing (Harbert et al., 2018; Salisbury et al., 2018; Walker & Allen, 2012).

Finally, there is an exception to the result that earthquake recurrence interval (i.e., many small earthquakes vs. few large earthquakes) and variance of the recurrence interval (i.e., periodic, semiperiodic, random, clustered earthquake histories) do not influence offset channel measurements. Offset channels from model runs with long intervals between earthquakes or long open intervals tend to underestimate modeled slip. This is

Table 1
Suggested Number of Offset Measurements From Population Statistics

σ of offset measurements (as fraction of total slip)[a]	Margin of error (as fraction of total slip)[b]	Confidence level [c]	Z^*[d]	*n*, number samples needed[e]
		99%	1.645	166
	0.1	95%	1.96	96
0.5		90%	2.576	68
		99%	1.645	42
	0.2	95%	1.96	24
		90%	2.576	17
		99%	1.645	60
	0.1	95%	1.96	35
0.3		90%	2.576	25
		99%	1.645	15
	0.2	95%	1.96	9
		90%	2.576	7
		99%	1.645	27
	0.1	95%	1.96	16
0.2		90%	2.576	11
		99%	1.645	7
	0.2	95%	1.96	4
		90%	2.576	3
		99%	1.645	7
	0.1	95%	1.96	4
0.1		90%	2.576	3
		99%	1.645	2
	0.2	95%	1.96	1
		90%	2.576	1

[a]If standard deviation is unknown, standard practice is to assume 0.5 [b]Uncertainty estimate is +/- half this value. [c]A 90% confidence level means there is a 90% chance the real mean is within the margin of error of the calculated mean for the given number of samples [d]Z^* value is from a Z table for stated confidence levels [e]Equation used to calculate: $n = (Z^* \sigma / \text{margin of error})^2$. This equation assumes the total population size is large or unknown. n is rounded up to the nearest integer.

apparent in models with recurrence intervals greater than ~3,000 years (Figures 5c and 5d) and $CV_{time} > 0.9$ that have clusters of earthquakes separated by long periods without slip (Figures 5e and 5f). For reasons discussed in section 4.3, we do not believe recurrence interval and CV_{time} are the causative variables in biasing mean measured offset, but instead, the existence of a long recurrence and/or open interval enables sufficient time for geomorphic evolution of the fault zone and channel shape postearthquake.

In summary, we find that for the geomorphic conditions modeled in this study, offset channels perpendicular to fault strike record cumulative modeled slip only when fault zone width is narrow, total offset is less than channel spacing, and the open interval is short. After accounting for differences in open intervals, there is no difference in offset distances between channels offset by periodic versus clustered earthquakes, nor is there a difference between channels offset by many small earthquakes versus few large earthquakes. In this numerical model setup, wider fault zones, longer open intervals, and cumulative slip greater than channel spacing all result in the average of offset channel measurements underestimating modeled slip.

4.2. Aleatoric Variance of Offsets

The large variability in individual offset measurements raises a number of questions for interpretation of slip measurements on strike-slip faults, such as the following: (1) How many offset measurements are needed to achieve a mean offset value that represents true slip? (2) If there are only a few offset measurements per fault section, what is the likelihood that these measurements represent true slip? And (3) how much variation in slip along strike can be attributed to aleatoric variance due to geomorphic irregularity (e.g., stream channel sinuosity), epistemic measurement uncertainty, and differences in seismic slip along strike?

Population statistics help answer some of these questions because the modeling experiments let us assess offset measurements against known slip history, and unlike typical paleoseismic studies that have 1–100 measurements, data sets from landscape evolution models have thousands of points. The number of samples

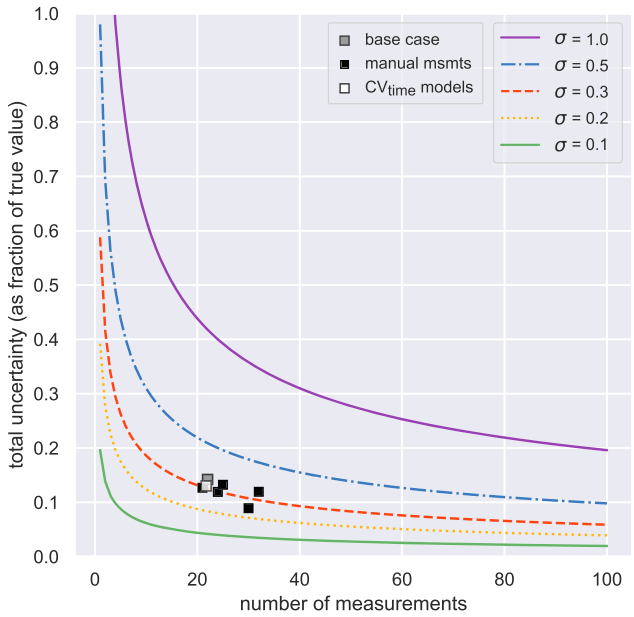

Figure 8. Theoretical total uncertainty (colored curves) at the 95% confidence level for different size sample populations and standard deviations (σ) compared to model data (squares). Offset measurements from numerical model runs (squares) show variability clustering around 30% (red dashed line) of modeled displacement. These data have ~10–15% total uncertainty (as percent of modeled slip), meaning there is a 95% chance that the measured mean is within 10–15% of modeled slip. The squares are the base case model (gray), the average of all models in the CV_{time} model set (white), and offset populations measured after each of five earthquakes in the model with a 2,000-year recurrence interval (black, individual data shown in Figure 11b). Note that σ for the theoretical curves is the same as $CV_{slip\text{-}spatial}$ because the calculations assume a mean of 1.

needed from a total population that is large or unknown for given standard deviations (σ), margins of error, and confidence levels is shown in Table 1. Confidence level assumes the sample population has a normal distribution around the true value. Margin of error is the uncertainty for a mean of measurements from that number of samples for a sample population with the given σ. Standard deviation here is shown normalized to total slip and is equal to $CV_{slip\text{-}spatial}$.

In this study, $CV_{slip\text{-}spatial}$ for the base case model is 0.34 (Figure 8), suggesting that 32–45 offset measurements are needed to be 90–95% sure the measured mean is within 10% of modeled slip, or 77 offset measurements are be needed to be 99% sure the measured mean is within 10% of modeled slip. If instead we consider that geologists will likely recognize large outlier measurements and exclude them, variability drops to 0.21 for the base case model. In that case, 12–17 measurements are needed to be 90–95% sure the measured mean is within 10% of modeled slip or 30 measurements to be 99% sure the measured mean is within 10% of modeled slip. These results suggest that minimum aleatoric variance is ~20% and can be >30% if outliers are included in the data set. Since modeled displacement can be recovered when outliers are included, we henceforth include all data in the discussion, which increases aleatoric variability but decreases subjective decisions.

Uncertainty calculations (colored curves) for theoretical numbers of samples and standard deviations at the 95% confidence level are shown in Figure 8 compared to model output (squares). From the figure, it is clear that $CV_{slip\text{-}spatial}$ measurements for multiple models cluster around ~30% variability (red dashed line). Note that σ is equal to CV for the theoretical sample populations because mean = 1 for the calculations. The figure shows that for a theoretical sample population with σ and CV = 0.3 (red dashed line), there is a 95% probability that one measurement is within ~60% of the true value. If we compare this to the CV_{time} model set, which has an average $CV_{slip\text{-}spatial}$ of 0.31 (Figure 8; Table S1), the odds are considerably worse. Only 82% of the 574 individual offset measurements from models in in the CV_{time} model set with CV_{time} <1 are within 60% of modeled displacement (Figure 5e). This difference may be because most models in the CV_{time} model set have open intervals at the end of the model run, which may cause measured mean offset to underestimate modeled displacement due to geomorphic change in the interim (see section 4.3). When measured mean underestimates true displacement, the sample population is skewed with respect to true displacement even though it is normally distributed around the measured mean.

However, the odds change if we consider mean measured offset instead of individual measurements. For the CV_{time} model set, 19–24 offset measurements are made per model, suggesting there is a 95% chance the measured mean offset is within ~13% of modeled displacement, and in this case the model results agree with the statistical expectation of capturing true displacement. In the CV_{time} model set, 96% of models have measured mean offset values within 13% of modeled displacement (Figures 5e and 5f). Thus, though individual offset measurements are variable and do not meet statistical expectations of capturing modeled displacement, mean measured offset for each model approximately records modeled displacement, even when outlier data are included.

The assumption underlying population statistics that one true value is recoverable with enough measurements (because they follow a normal distribution around the true value) may not be valid for all surface rupture studies for two reasons. First, there may not be one true mean because real variation in slip at the surface is common in a single earthquake (e.g., Choi et al., 2012, 2018; Gold et al., 2013; Gold et al., 2015; Milliner et al., 2015; Quigley et al., 2012; Rockwell et al., 2002 & 2013; Zielke et al., 2015) and through multiple earthquake cycles (e.g., Haddon et al., 2016; Zielke et al., 2012; Zielke et al., 2015). Second, the normal distribution in offset measurements for historical and paleoseismic slip distributions may not center on

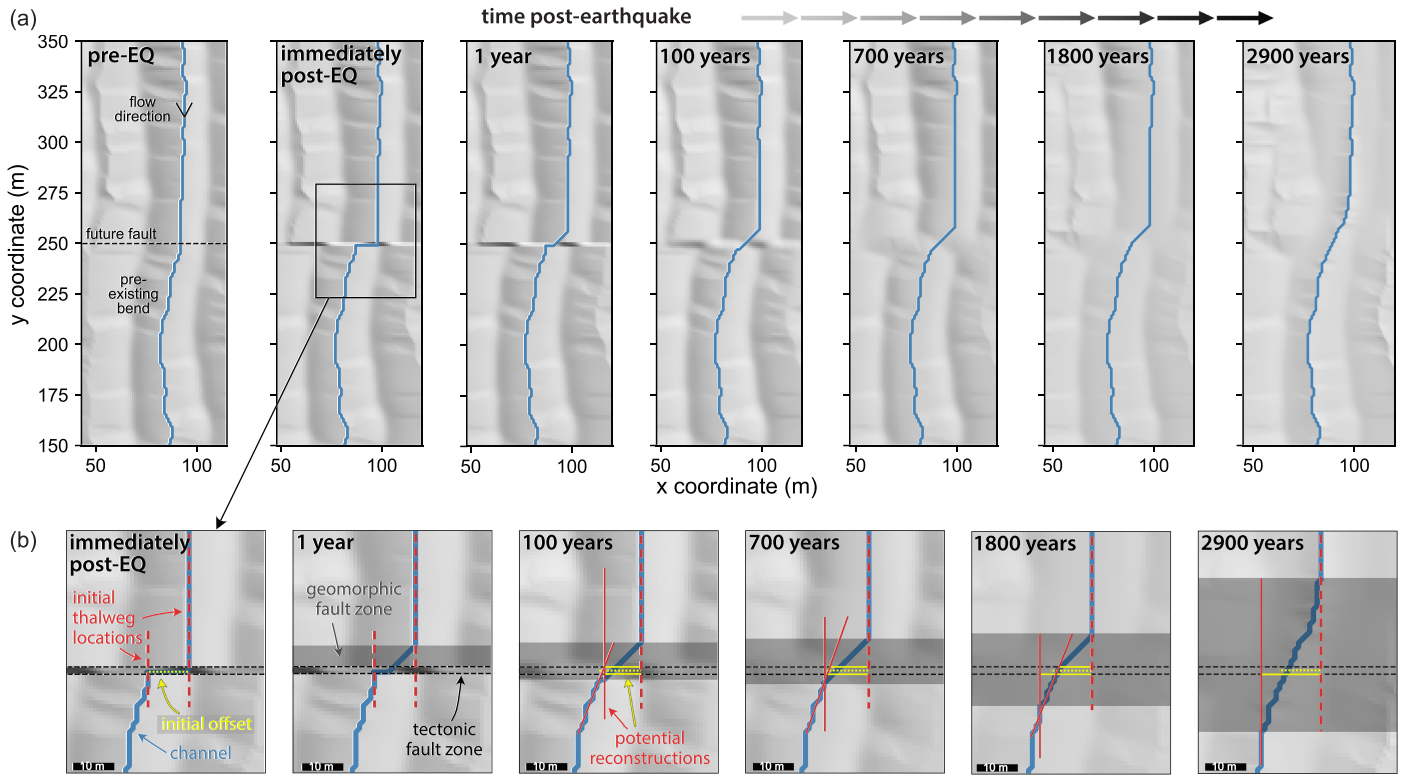

Figure 9. Fault zone and channel evolution from a model run with one 10-m-slip earthquake on a discrete fault plane every 3,000 years, no prior lateral displacement, and ~30-m channel spacing. (a) Uninterpreted and (b) interpreted map view of an example channel (blue line) shown on a hillshade image of the surrounding landscape prior to the earthquake, immediately after the earthquake, and in subsequent years. The widths of the geomorphic (gray shading) and tectonic (dashed black lines) fault zones are illustrated in (b). The first panel of (b) shows the initial postearthquake locations of the thalwegs (red dashed lines) and offset (yellow dotted line). Subsequent panels show a range of possible reconstructions (solid lines) compared to the initial offset (yellow dotted line).

true displacement because offset measurements may systematically underestimate true displacement when geomorphic modification has occurred (see section 4.3).

Thus, we should consider the aleatoric variance in individual offset measurements in addition to tectonic variation in slip along strike and epistemic measurement uncertainty when interpreting populations of offset measurements, both for single-earthquake and multiple-event populations. Although most geologists will recognize large offset measurements that result from stream captures as outliers after a recent earthquake, these large offsets may be less obvious as outliers after multiple earthquakes have occurred. Furthermore, measurements that overestimate actual displacement per event can result from preexisting channel sinuosity or morphology, causing large measurement uncertainty. Since mean measured offset tracks modeled displacement under certain conditions in the numerical models, our results suggest that averaging multiple measurements when calculating slip distribution for individual fault sections after recent earthquakes can reasonably approximate true displacement while diminishing some of the aleatoric and epistemic variability in individual offset measurements.

4.3. The Geomorphic Fault Zone

An implicit assumption in correlating channels across a fault is that the correlated marker has remained relatively static since the earthquake, whether the marker is a channel thalweg, a profile across a thalweg, or a channel margin. This is a false assumption because channels—including channel thalwegs and cross-channel profiles—are not static, as demonstrated visually (Figure 9) and quantitatively (Figure 7) by our numerical models, field investigation on the San Andreas Fault (Lienkaemper & Strum, 1989; Salisbury et al., 2018), and analog flume experiments (Ouchi, 2004). In flume experiments, Ouchi (2004) found that streams responded to lateral displacement with upstream aggradation, downstream degradation, and lateral shifting. Lienkaemper and Strum (1989) investigated a laterally offset stream on the San Andreas Fault from

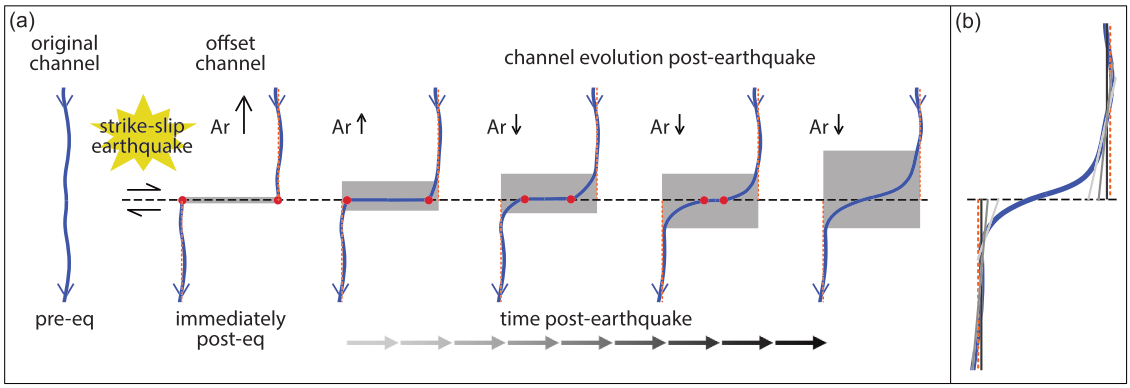

Figure 10. Conceptual model of postearthquake offset channel evolution based on landscape evolution models of lateral displacement. (a) Offset channel evolution postearthquake. The geomorphic fault zone (zone of apparent offset, gray shading) widens orthogonal to the fault, and the initially discrete channel offset (red circles) is eroded as time passes postearthquake. Orange dashed lines show the initial displacement and are the same distance apart in all depictions of the offset channel. (b) The final offset channel with potential reconstructions of the offset shown in black to shades of gray. Most reconstructions underestimate true displacement, which is illustrated with orange dashed lines.

aerial photos taken 20 years apart and found 1 m of sediment deposited on the steeper bank of the channel, and little incision, making the offset appear ~2 m smaller than after the earthquake. These examples illustrate a few of the ways that offset channels can be altered by geomorphic processes postearthquake, and our models corroborate that apparent channel offsets result from a combination of tectonic offset and geomorphic response since the earthquake (Lienkaemper & Strum, 1989; Salisbury et al., 2018; Wallace, 1968; Zielke, 2018; Zielke et al., 2015).

To describe this postearthquake fault zone evolution, we present the idea of the "geomorphic fault zone" (gray-shaded region in Figures 9 and 10), the zone of apparent offset that evolves throughout the earthquake cycle. It is distinct from the tectonic fault zone, which is the zone of coseismic distributed deformation (FZW in our models). In our models with 0-m FZW, all coseismic deformation occurs on the fault, but the zone of apparent offset, the geomorphic fault zone, is wider and grows with time.

We illustrate the development of the geomorphic fault zone using the model with a 3,000-year earthquake recurrence interval (and 0-m FZW) because the long recurrence makes observation easier (Figure 9). The process is also shown conceptually in Figure 10. Snapshots in time after the first earthquake, with 10-m displacement, illustrate channel evolution postearthquake (Figure 9). The offset in the channel thalweg (yellow dotted line in Figure 9b) is straight and discrete immediately postearthquake, but over time the discrete offset becomes diminished as the 90° bends are smoothed. The gray shading in Figure 9b shows the evolution of the geomorphic fault zone for this example channel. While immediately after the earthquake the geomorphic and tectonic fault zones are identical, as the landscape evolves, the transition zone from offset to non-offset thalweg migrates up and down the channel (Figure 9), extending the zone of apparent offset. This results in widening of the geomorphic fault zone and reducing the apparent offset as the upstream and downstream portions of the channel evolve. Solid yellow lines illustrate potential offset measurements at various times postearthquake defined by projections of the channel thalweg into the fault (solid red lines) as compared to the initial offset (dotted yellow line). These reconstructions can overestimate or underestimate modeled displacement from the most recent earthquake depending on channel orientation and morphology and decisions made by the user. Note that in this particular case, offset reconstructions based on projecting an average thalweg location into the fault tend to overestimate modeled displacement due to a preexisting bed in the channel morphology (Figure 9a).

Geomorphic fault zone evolution is also observed in the orientation of fault zone topography as quantified by Ar (Figure 7) and is especially evident in the model with a 3,000-year recurrence interval (Figure 7d). After each earthquake, Ar of the fault zone initially increases but then decreases with time, as fault zone topography initially becomes more fault parallel and then evolves in a fault-perpendicular orientation. The initial increase in fault-parallel topography (Ar increase) likely is due to erosion along the fault, possibly of interfluve margins, in the years following the earthquake (Figures 7d and 9, 1–700+ years

postearthquake). The subsequent increase in fault-perpendicular topography (Ar decrease) coincides with the widening of the geomorphic fault zone and straightening of the offset channel (Figures 7d and 9). Thus, both orientation of fault zone topography and evolution of individual channels in landscape evolution models suggest that postearthquake channel evolution modifies apparent offset marker distance. With further work to constrain climate and lithologic influences, this relationship may allow time since the last earthquake to be assessed from fault zone geomorphology, as with normal fault scarps and well-defined diffusion coefficients.

A conceptual model of postearthquake offset channel evolution is presented in Figure 10 for channels perpendicular to fault strike. Immediately following the earthquake, incision and erosion happen along the fault, increasing the proportion of fault-parallel topography (Ar increase). In subsequent years, the geomorphic fault zone widens orthogonal to the fault, and the discrete offset is smeared, decreasing fault-parallel topography and Ar. In the conceptual model, thalweg locations far from the fault remain stationary, but the numerical model does not included lateral erosion and stream migration (Langston & Tucker, 2018) and therefore likely understates the degree of lateral channel mobility (Kwang & Parker, 2019). Ouchi (2004) found that thalweg locations can migrate laterally in flume experiments of faulted channels. Though beyond the scope of this study, the rate and style of this process likely depend on climate, and lithology of the fault zone landscape and further modeling is required to define how this might occur. Comparing these results to those of Duvall and Tucker (2015) and Harbert et al. (2018) indicates that the strength of the faulted material (i.e., lithology) may fundamentally control some aspects of fault zone evolution.

4.4. Limitations and Their Implications

One primary conclusion is that the mean of multiple offset channel measurements underestimates modeled displacement if the elapsed time between earthquake and offset measurement is sufficient for growth of the geomorphic fault zone and modification of discrete channel offsets (Figures 5 and 10). In section 2.3.1 and Figure 4, we show that both automatic thalweg matching measurements and linear projections by humans underestimate modeled displacement as fault zone width increases, but automatic measurements underestimate modeled displacement more than human measurements. While the magnitude of the observed underestimation may be enhanced by the automatic measurement method, we remain confident that the existence of the underestimation is not due to measurement limitation in these numerical models.

This illustrates one of the primary decisions made when measuring offset channels across a fault: deciding on an appropriate location upstream and downstream of the fault to measure offset. A location too close to the fault (i.e., within the geomorphic fault zone) may result in underestimating true displacement, but at locations far from the fault, it may not be possible to separate tectonic offset from channel sinuosity. As the fault zone and channel offset evolve postearthquake, it will become more difficult to determine the best location for the measurement profile. This decision is not unique to the automatic measurement method. Both matching thalwegs at a point and correlating channel cross-profiles require deciding where to take the measurement normal to the fault. No matter the approach, the pre-earthquake channel morphology is more difficult to discern after a long open interval. Though the magnitude of this problem may depend on climatic and lithologic conditions, uncertainty in a measurement is inherently greater with more elapsed time between earthquake and measurement.

Future studies may systematically explore the development and response of offset landforms under varying lithologic, climatic, and topographic conditions. For this investigation, we assess the sensitivity of the current model to different values of K and D with a sensitivity analysis of the base case conditions (0-m FZW and 15 periodic earthquakes of 2 m each), and we found no significant difference in offset measurements (Figure S3). While future versions of the model will include deposition by surface flow (Shobe et al., 2017) and multiple flow direction routing (e.g., Tarboton, 1997), we expect these improvements will only increase variability and uncertainty in offset measurements because they will likely cause channels to be less entrenched and meander more than they do in the current model. Furthermore, though a more complex numerical model may better represent natural conditions, it creates a larger parameter space and thus makes the results harder to understand, interpret, and compare to real faults.

4.5. Implications for Identifying, Measuring, and Interpreting Offset Channels

The results of this study suggest criteria for correlating, measuring, and interpreting offset channels. When correlating offset channels, future work should be mindful of how much slip has occurred since the offset landform was created and how that amount of displacement relates to channel spacing. If total slip is much larger than channel spacing (i.e., in measurements of cumulative displacement for geologic slip rate studies), then it is unlikely the channels can be correlated confidently, unless other factors (e.g., dates, lithologic differences, or variations in channel size) support the correlation. Second, the elapsed time since the earthquake should be considered to gauge how much channel and fault zone modification has occurred. If the open interval is long for the climatic and lithologic conditions, then substantial channel modification may have happened, and offset channels may not record full displacement of past events. Finally, as demonstrated in Figures 9 and 10, the width of the geomorphic fault zone and the width of the tectonic fault zone are not the same, and the width of the geomorphic fault zone increases postearthquake.

Channel offsets measured near a fault may tend toward underestimating true displacement as the geomorphic fault zone widens and the discrete offset smears postearthquake. In order to avoid missing part of the displacement, long sections of thalwegs (or other linear features) should be used that can be projected into the fault. However, it can be difficult to determine where to take an average thalweg location because channels meander—much more so than in numerical models (Kwang & Parker, 2019)—and this problem becomes more pronounced for longer periods since an earthquake. Uncertainties in how a linear feature is projected into the fault are measurement uncertainty. One study of measurement uncertainty found 11–12% variation in repeat measurements of offset features after the 2010 El Mayor Cucapah earthquake (Gold et al., 2013). Lateral shifting of the thalweg postearthquake was not a factor in that study due to dry conditions, but in wetter conditions or with more time since an earthquake, geomorphic change could further increase uncertainty. Since fault zone landscape evolution and reorganization introduce aleatoric variation, longer periods of elapsed time since an earthquake introduce greater uncertainty in the pre-earthquake and immediate postearthquake position and morphology of an offset channel. Perhaps slip rates derived from offset markers should include uncertainty based on the latency between the earthquake and when the offset was measured, though some of this may be inherently incorporated in measurement uncertainty.

The thousands of offset measurements recorded in this study let us infer best practices for interpreting populations of offset measurements from recent earthquakes. Our analysis shows that even with ~30% variability in offset measurements, modeled slip is recovered by averaging multiple measurements (Figures 5 and 11a). As might be expected, this work and population statistics imply that more measurements are better than fewer, ideally with 25–35 per fault section of interest (Table 1). Similarly, results show that model outliers are not reliable measurements of displacement and are unrelated to modeled slip. Anomalously large offsets ($>2\sigma$ from the mean) can result from stream captures, which may or may not be obvious. Thus, multiple offset measurements should be averaged and smoothed within a fault section to estimate true slip, and interpreting small variations in slip along strike should be avoided.

This natural variability in individual offset measurements from one earthquake (e.g., Figure 11a) may make offset measurements appear clustered, leading to incorrect interpretation of the number and/or sizes of paleoseismic earthquakes. For example, the data shown in Figure 11a were collected after one earthquake, but the distribution of offset measurements may be interpreted to represent two to three earthquakes (Figure 11a, left panel). The mean offset, however, approximately records modeled slip (10 m) and is more obvious when data are plotted cumulatively (Figure 11a, right panel). Apparent clustering is especially problematic when slip is greater than channel spacing, causing apparent offset measurements to be less than cumulative slip (Figures 5g and 5h and Salisbury et al., 2018; Walker & Allen, 2012), or if stream captures cause some offset measurements to be approximately double true slip (Figures 5c and 5e). If only a few measurements are possible or outliers are included, the spread of offset measurements from recent events may be misinterpreted as evidence for prior events.

Variability is even harder to interpret when multiple earthquakes have occurred, overprinting prior offsets in the landscape. Figure 11b shows manual offset measurements made after each of five earthquakes in the model with a 2,000-year recurrence interval and 6-m slip per earthquake. The measurements are grouped by the amount of cumulative slip in the model when they were measured (Figure 11b, middle),

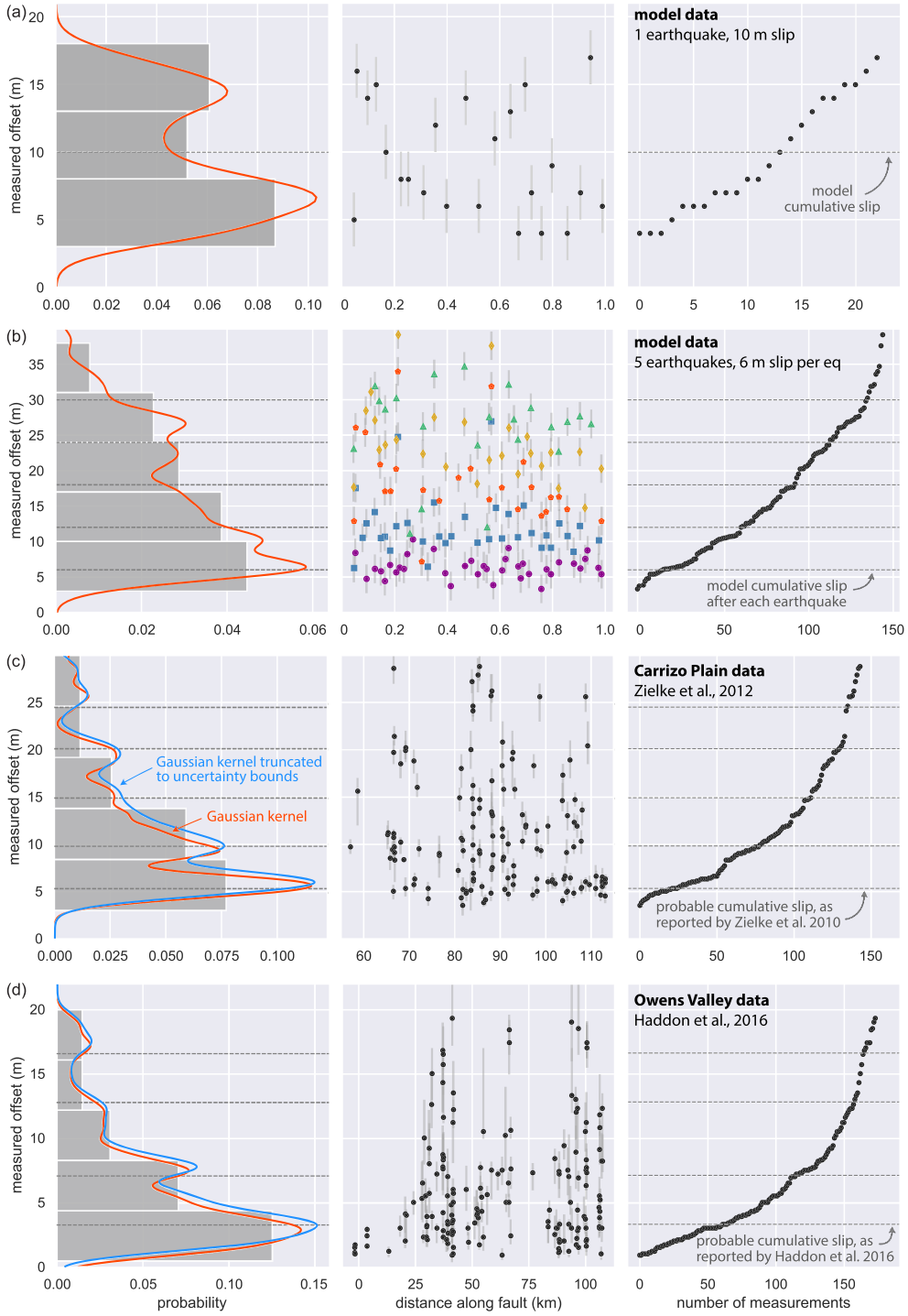

Figure 11. Offset measurements from numerical models (a and b) and real faults (c and d). Left panels are offset measurement density plotted as histograms and kernel density estimates (KDEs). Red lines are KDEs constructed from purely Gaussian kernels. Blue lines are KDEs constructed from Gaussian kernels clipped to minimum and maximum of measurement uncertainty for each data point (gray error bars in middle panel). Both curves are constructed from the entire data set. Middle panels are offset measurements and their uncertainty estimates. Right panels are offset measurements plotted cumulatively from smallest to largest. (a) Offsets from a numerical model with one 10-m-slip earthquake measured automatically immediately following the earthquake. (b) Offsets from a numerical model with five earthquakes and 6-m slip per earthquake measured manually after each earthquake. Markers are grouped by cumulative slip when measured. Offset measurements from (c) the Carrizo Plain section of the San Andreas Fault for the 1857 and previous earthquakes (data from Zielke et al., 2012), and (d) Owens Valley from the 1872 and previous earthquakes (data from Haddon et al., 2016). Dashed lines are cumulative modeled slip in (a) and (b) and interpreted cumulative offset from cumulative offset probability density (COPD) analysis of offset measurements from historical and paleoseismic earthquakes by Zielke et al. (2010) in (c) and Haddon et al. (2016) in (d).

in order to compare with real datasets of multiple earthquakes from the paleoseismic record (Figures 11c and 11d). The variability in modeled offset measurements causes overprinting and illustrates that clusters can emerge that do not relate to tectonic history. From the density of these data (red line in Figure 11b, left panel), four to seven previous earthquakes could be interpreted, but only the first peak corresponds to modeled cumulative slip. Model results (Figure 11b) corroborate observations (Figures 11c and 11d and Haddon et al., 2016; Salisbury et al., 2012; Zielke et al., 2012) that displacement peaks are rarely well resolved for events prior to the most recent earthquake. Carrizo Plain and Owens Valley data (Figures 11c and 11d) demonstrate that a short recurrence interval or different slip rates do not help this issue. Therefore, we echoe previous studies (Salisbury et al., 2018) in emphasizing the need to date individual offset measurements and question the practice of interpreting the number and size of paleoseismic earthquakes from populations of apparently clustered offset measurements .

5. Conclusion

We used landscape evolution models to explore how offset channels and fault zone geomorphology of a theoretical strike-slip landscape respond to varying four tectonic parameters: (1) fault zone width (zone of coseismic distributed deformation), (2) earthquake recurrence interval (many small vs. few large earthquakes), (3) variance of the recurrence interval (periodic, semiperiodic, random, and clustered earthquake histories), and (4) total slip in relation to channel spacing. Models ran for 10 ka to simulate multiple earthquake cycles under uniform and steady uplift, erosion, and diffusion conditions. From analysis of model output, we find the following:

1. Individual offset measurements are variable, often encompassing ~30% of mean slip. While modeled slip can be recovered by taking the average offset of multiple measurements, individual measurements are unlikely to accurately record modeled slip.
2. Average offset measurements from channels perpendicular to fault strike underestimate modeled slip except when the fault zone is narrow (less than ~5 m), total offset is less than channel spacing, and offsets are measured quickly following the last earthquake.
3. Initial channel spacing is a primary control on the maximum offset distance recorded by channels, and channels offset more than the distance between them do not accurately record tectonic slip. In the natural world, however, correlations may be possible with additional controls such as dates and/or variations in lithology or channel size.
4. We define the geomorphic fault zone as the zone of apparent offset, which is distinct from the tectonic fault zone, or zone of coseismic distributed deformation.
5. Postearthquake landscape evolution widens the geomorphic fault zone and diminishes apparent channel offset distances in the models as the initially discrete offset is smeared.
6. Individual offset measurement variability can cause populations of offset measurements to appear clustered in a manner that does not reflect the modeled earthquake history. Similar patterns observed along real faults have been interpreted as evidence of multiple surface-rupturing earthquakes.

In conclusion, our results confirm the importance of immediate postearthquake field investigation and remote data collection of the entire fault zone, as well as making multiple offset measurements and averaging data within fault sections. This study underscores the importance of considering degradation due to geomorphic evolution when interpreting offset markers (especially if only a few markers are measured or a long time has elapsed since the earthquake occurred) and urges caution interpreting complex slip histories from multiple earthquakes in paleoseismic studies. We also demonstrate the utility of landscape evolution models to experimentally explore conditions not easily defined for natural faults, and raise more questions to address. For example, how much of the observed along-strike variability immediately postearthquake is due to tectonic versus geomorphic factors? And, how do climate and lithology regulate postearthquake fault zone evolution?

Acknowledgments
Thanks to Katherine Scharer, two anonymous reviewers, and the Associate Editor for their constructive comments that strengthened and clarified the manuscript. Strike-slip model code, offset measurement code, and input parameter values for all model runs are available via an open-access repository (DOI: 10.5281/zenodo.3374026). This material is based on work supported by the National Science Foundation Graduate Research Fellowship Program under Grant DGE-1650115 and an internship provided by the Graduate Research Internship Program to N. R. K. B. acknowledges an NSF EAR Postdoctoral Fellowship (EAR-1725774). This work utilized the RMACC Summit supercomputer, which is supported by the National Science Foundation (Awards ACI-1532235 and ACI-1532236), the University of Colorado Boulder, and Colorado State University. The Summit supercomputer is a joint effort of the University of Colorado Boulder and Colorado State University.

References

Amos, C. B., Audet, P., Hammond, W. C., Burgmann, R., Johanson, I. A., & Blewitt, G. (2014). Uplift and seismicity driven by groundwater depletion in central California. *Nature*, *509*(7501), 483–486. https://doi.org/10.1038/nature13275

Binet, R., & Bollinger, L. (2005). Horizontal coseismic deformation of the 2003 Bam (Iran) earthquake measured from SPOT-5 THR satellite imagery. *Geophysical Research Letters*, *32*, L02307. https://doi.org/10.1029/2004GL021897

Bollinger, L., Perrier, F., Avouac, J. P., Sapkota, S., Gautam, U., & Tiwari, D. R. (2007). Seasonal modulation of seismicity in the Himalaya of Nepal. *Geophysical Research Letters*, *34*, 1–5. https://doi.org/10.1029/2006GL029192

Brothers, D., Kilb, D., Luttrell, K., Driscoll, N., & Kent, G. (2011). Loading of the San Andreas Fault by flood-induced rupture of faults beneath the Salton Sea. *Nature Geoscience*, *4*(7), 486–492. https://doi.org/10.1038/ngeo1184

Burbank, D. W., & Anderson, R. S. (2012). *Tectonic geomorphology*. West Sussex: Wiley-Blackwell. https://doi.org/10.1002/9781444345063

Calais, E., Freed, A. M., Van Arsdale, R., & Stein, S. (2010). Triggering of New Madrid seismicity by late-Pleistocene erosion. *Nature*, *466*(7306), 608–611. https://doi.org/10.1038/nature09258

Caskey, S. J., & Wesnousky, S. G. (1997). Static stress changes and earthquake triggering during the 1954 Fairview Peak and Dixie Valley earthquakes, central Nevada. *Bulletin of the Seismological Society of America*, *87*, 521–527.

Choi, J.-H., Jin, K., Enkhbayar, D., Davvasambuu, B., Bayasgalan, A., & Kim, Y. (2012). Rupture propagation inferred from damage patterns, slip distribution, and segmentation of the 1957 Mw8.1 Gobi-Altay earthquake rupture along the Bogd fault, Mongolia. *Journal of Geophysical Research*, *117*, 1–24. https://doi.org/10.1029/2011JB008676

Choi, J.-H., Klinger, Y., Ferry, M., Ritz, J.-F., Kurtz, R., Rizza, M., et al. (2018). Geologic inheritance and earthquake rupture processes: The 1905 M ≥ 8 Tsetserleg-Bulnay strike-slip earthquake sequence, Mongolia. *Journal of Geophysical Research: Solid Earth*, *123*, 1925–1953. https://doi.org/10.1002/2017JB013962

Delong, S. B., Donnellan, A., Ponti, D. J., Rubin, R. S., Lienkaemper, J. J., Prentice, C. S., et al. (2016). Tearing the terroir: Details and implications of surface rupture and deformation from the 24 August 2014 M6.0 South Napa earthquake, California Stephen. *Earth and Space Science*, *3*, 1–15. https://doi.org/10.1002/2016EA000176.Received

DuRoss, C. B., Personius, S. F., Crone, A. J., Olig, S. S., Hylland, M. D., Lund, W. R., & Schwartz, D. P. (2016). Fault segmentation: New concepts from the Wasatch Fault Zone, Utah, USA. *Journal of Geophysical Research: Solid Earth*, *121*, 1–27. https://doi.org/10.1002/2015JB012519.Received

Duvall, A. R., & Tucker, G. E. (2015). Dynamic ridges and valleys in a strike-slip environment. *Journal of Geophysical Research: Earth Surface*, *120*, 2016–2026. https://doi.org/10.1002/2015JF003618

Ellsworth, W. L. (2013). Injection-induced earthquakes. *Science*, *341*, 1–8.

Fletcher, J. M., Teran, O. J., Rockwell, T. K., Oskin, M. E., Hudnut, K. W., Mueller, K. J., et al. (2014). Assembly of a large earthquake from a complex fault system: Surface rupture kinematics of the 4 April 2010 El Mayor-Cucapah (Mexico) Mw 7.2 earthquake. *Geosphere*, *10*(4), 797–827. https://doi.org/10.1130/GES00933.1

Frankel, K. L., Brantley, K. S., Dolan, J. F., Finkel, R. C., Klinger, R. E., Knott, J. R., et al. (2007). Cosmogenic 10Be and 36Cl geochronology of offset alluvial fans along the northern Death Valley fault zone: Implications for transient strain in the eastern California shear zone. *Journal of Geophysical Research*, *112*, 1–18. https://doi.org/10.1029/2006JB004350

Frankel, K. L., Dolan, J. F., Finkel, R. C., Owen, L. A., & Hoeft, J. S. (2007). Spatial variations in slip rate along the Death Valley-Fish Lake Valley fault system determined from LiDAR topographic data and cosmogenic10Be geochronology. *Geophysical Research Letters*, *34*, 1–6 . https://doi.org/10.1029/2007GL030549

Frankel, K. L., Dolan, J. F., Owen, L. A., Ganev, P., & Finkel, R. C. (2011). Spatial and temporal constancy of seismic strain release along an evolving segment of the Pacific-North America plate boundary. *Earth and Planetary Science Letters*, *304*, 565–576. https://doi.org/10.1016/j.epsl.2011.02.034

Ge, S., Liu, M., Lu, N., Godt, J. W., & Luo, G. (2009). Did the Zipingpu Reservoir trigger the 2008 Wenchuan earthquake? *Geophysical Research Letters*, *36*, 1–5. https://doi.org/10.1029/2009GL040349

Gold, P. O., Oskin, M. E., Elliott, A. J., Hinojosa-Corona, A., Taylor, M. H., Kreylos, O., & Cowgill, E. (2013). Coseismic slip variation assessed from terrestrial lidar scans of the El Mayor-Cucapah surface rupture. *Earth and Planetary Science Letters*, *366*, 151–162. https://doi.org/10.1016/j.epsl.2013.01.040

Gold, R. D., Reitman, N. G., Briggs, R. W., Barnhart, W. D., Hayes, G. P., & Wilson, E. (2015). On- and off-fault deformation associated with the September 2013 Mw 7.7 Balochistan earthquake: Implications for geologic slip rate measurements. *Tectonophysics*, *660*, 65–78. https://doi.org/10.1016/j.tecto.2015.08.019

González, P. J., Tiampo, K. F., Palano, M., Cannavó, F., & Fernández, J. (2012). The 2011 Lorca earthquake slip distribution controlled by groundwater crustal unloading. *Nature Geoscience*, *5*, 821–825. https://doi.org/10.1038/ngeo1610

Grant Ludwig, L., Akciz, S. O., Noriega, G. R., Zielke, O., & Arrowsmith, J. R. (2010). Climate-modulated channel incision and rupture history of the San Andreas fault in the Carrizo Plain. *Science*, *327*(5969), 1117–1119. https://doi.org/10.1126/science.1182837

Gray, H. J., Shobe, C. M., Hobley, D. E. J., Tucker, G. E., Duvall, A. R., Harbert, S. A., & Owen, L. A. (2018). Off-fault deformation rate along the southern San Andreas fault at Mecca Hills, southern California, inferred from landscape modeling of curved drainages. *Geology*, *46*(1), 59–62. https://doi.org/10.1130/G39820.1

Haddon, E. K., Amos, C. B., Zielke, O., Jayko, A. S., & Burgmann, R. (2016). Surface slip during large Owens Valley earthquakes. *Geochemistry, Geophysics, Geosystems*, *17*, 2239–2269. https://doi.org/10.1002/2015GC006033

Hampel, A., Hetzel, R., & Densmore, A. L. (2007). Postglacial slip-rate increase on the Teton normal fault, northern Basin and Range Province, caused by melting of the Yellowstone ice cap and deglaciation of the Teton Range? *Geology*, *35*, 1107–1110. https://doi.org/10.1130/G24093A.1

Harbert, S. A., Duvall, A. R., & Tucker, G. E. (2018). The role of near-fault relief elements in creating and maintaining a strike-slip landscape. *Geophysical Research Letters*, *45*, 11,683–11,692. https://doi.org/10.1029/2018GL080045

Hill, D. P., Reasenberg, A., Michael, A., Arabaz, W. J., Beroza, G., Brumbaugh, D., et al. (1993). Seismicity remotely triggered by the magnitude 7.3 Landers, California, earthquake. *Science*, *260*(5114), 1617–1623. https://doi.org/10.1126/science.260.5114.1617

Hobley, D. E. J., Adams, J. M., Siddhartha Nudurupati, S., Hutton, E. W. H., Gasparini, N. M., Istanbulluoglu, E., & Tucker, G. E. (2017). Creative computing with Landlab: An open-source toolkit for building, coupling, and exploring two-dimensional numerical models of Earth-surface dynamics. *Earth Surface Dynamics*, *5*, 21–46. https://doi.org/10.5194/esurf-5-21-2017

Hodgkinson, K. M., Stein, R. S., & King, G. C. P. (1996). The 1954 Rainbow Mountain-Fairview Peak-Dixie Valley earthquakes: A triggered normal faulting sequence. *Journal of Geophysical Research*, *101*(B11), 25,459–25,471. https://doi.org/10.1029/96JB01302

Kagan, Y. Y., & Jackson, D. D. (1991). Long-term earthquake clustering. *Geophysical Journal International*, *104*(1), 117–134. https://doi.org/10.1111/j.1365-246X.1991.tb02498.x

Kilb, D., Gomberg, J., & Bodin, P. (2000). Triggering of earthquake aftershocks by dynamic stresses. *Nature*, *408*(6812), 570–574. https://doi.org/10.1038/35046046

Klinger, Y., Etchebes, M., Tapponnier, P., & Narteau, C. (2011). Characteristic slip for five great earthquakes along the Fuyun fault in China. *Nature Geoscience*, *4*(6), 389–392. https://doi.org/10.1038/ngeo1158

Klinger, Y., Xu, X., Tapponnier, P., Lasserre, C., & King, G. (2005). High-resolution satellite imagery mapping of the surface rupture and slip distribution of the Mw ~7.8, 14 November 2001 Kokoxili earthquake, Kunlun fault, northern Tibet, China. *Bulletin of the Seismological Society of America*, *95*, 1970–1987. https://doi.org/10.1785/0120040233

Koehler, R. D., & Wesnousky, S. G. (2011). Late Pleistocene regional extension rate derived from earthquake geology of late Quaternary faults across the Great Basin, Nevada, between 38.5° N and 40° N latitude. *Geological Society of America Bulletin*, *123*, 631–650. https://doi.org/10.1130/B30111.1

Kwang, J. S., & Parker, G. (2019). Extreme memory of initial conditions in numerical landscape evolution models. *Geophysical Research Letters*, *46*, 6563–6573. https://doi.org/10.1029/2019GL083305

Langston, A. L., & Tucker, G. E. (2018). Developing and exploring a theory for the lateral erosion of bedrock channels for use in landscape evolution models. *Earth Surface Dynamics*, *6*(1), 1–27. https://doi.org/10.5194/esurf-6-1-2018

Lee, J., Spencer, J., & Owen, L. (2001). Holocene slip rates along the Owens Valley fault, California: Implications for the recent evolution of the Eastern California Shear Zone. *Geology*, *29*, 819–822. https://doi.org/10.1130/0091-7613(2001)029<0819:HSRATO>2.0.CO;2

Lienkaemper, J. J., & Strum, T. A. (1989). Reconstruction of a channel offset in 1857(?) by the San Andreas fault near Cholame, California. *Bulletin of the Seismological Society of America*, *79*, 901–909.

Massonnet, D., Rossi, M., Carmona, C., Adragna, F., Peltzer, G., Feigl, K. L., & Rabaute, T. (1993). The displacement field of the Landers earthquake mapped by radar interferometry. *Nature*, *364*(6433), 138–142. https://doi.org/10.1038/364138a0

Milliner, C. W. D., Dolan, J. F., Hollingsworth, J., Leprince, S., Ayoub, F., & Sammis, C. G. (2015). Quantifying near-field and off-fault deformation patterns of the 1992 Mw 7.3 Landers earthquake. *Geochemistry, Geophysics, Geosystems*, *16*, 1577–1598. https://doi.org/10.1002/2014GC005693

Okada, Y. (1985). Surface deformation due to shear and tensile faults in a half-space. *Bulletin of the Seismological Society of America*, *75*, 1135–1154.

Ouchi, S. (2004). Flume experiments on the horizontal stream offset by strike-slip faults. *Earth Surface Processes and Landforms*, *29*, 161–173. https://doi.org/10.1002/esp.1017

Pérouse, E., & Wernicke, B. P. (2017). Spatiotemporal evolution of fault slip rates in deforming continents: The case of the Great Basin region, northern Basin and Range province. *Geosphere*, *13*, 112–135. https://doi.org/10.1130/GES01295.1

Quigley, M., Van Dissen, R., Litchfield, N., Villamor, P., Duffy, B., Barrell, D., et al. (2012). Surface rupture during the 2010 Mw 7.1 Darfield (Canterbury) earthquake: Implications for fault rupture dynamics and seismic-hazard analysis. *Geology*, *40*(1), 55–58. https://doi.org/10.1130/G32528.1

Reheis, M. C., & Sawyer, T. L. (1997). Late Cenozoic history and slip rates of the Fish Lake Valley, Emigrant Peak, and Deep Springs fault zones, Nevada and California. *Bulletin of the Geological Society of America*, *109*, 280–299. https://doi.org/10.1130/0016-7606(1997)109

Reitman, N.G., Mueller, K.J., Tucker, G.E., Gold, R.D., Briggs, R.W., and Barnhart, K.R., 2019, Numerical model code and input files to run landscape evolution models with strike-slip faulting and measure channel offsets. https://doi.org/10.5281/zenodo.3374026.

Rockwell, T. K., & Klinger, Y. (2013). Surface rupture and slip distribution of the 1940 Imperial Valley earthquake: Imperial fault, southern California: Implications for rupture segmentation and dynamics. *Bulletin of the Seismological Society of America*, *103*, 629–640. https://doi.org/10.1785/0120120192

Rockwell, T. K., Lindvall, S., Dawson, T., Langridge, R., Lettis, W., & Klinger, Y. (2002). Lateral offsets on surveyed cultural features resulting from the 1999 Izmit and Duzce earthquakes, Turkey. *Bulletin of the Seismological Society of America*, *92*, 79–94. https://doi.org/10.1785/0120000809

Salisbury, J. B., Arrowsmith, J. R., Brown, N., Rockwell, T., Akciz, S., & Ludwig, L. G. (2018). The age and origin of small offsets at Van Matre Ranch along the San Andreas fault in the Carrizo Plain, California. *Bulletin of the Seismological Society of America*, *108*, 639–653. https://doi.org/10.1785/0120170162

Salisbury, J. B., Rockwell, T. K., Middleton, T. J., & Hudnut, K. W. (2012). LiDAR and field observations of slip distribution for the most recent surface ruptures along the central San Jacinto fault. *Bulletin of the Seismological Society of America*, *102*, 598–619. https://doi.org/10.1785/0120110068

Savage, J. C., & Burford, R. O. (1973). Geodetic determination of relative plate motion in central California. *Journal of Geophysical Research*, *78*(5), 832–845. https://doi.org/10.1029/JB078i005p00832

Scharer, K., Weldon, R., Biasi, G., Streig, A., & Fumal, T. (2017). Ground-rupturing earthquakes on the northern Big Bend of the San Andreas Fault, California, 800A.D. to Present. *Journal of Geophysical Research: Solid Earth*, *122*, 2193–2218. https://doi.org/10.1002/2016JB013606

Schwartz, D. P. (2018). Review: Past and future fault rupture lengths in seismic source characterization—The long and short of It. *Bulletin of the Seismological Society of America*, *108*, 2493–2520. https://doi.org/10.1785/0120160110

Shobe, C. M., Tucker, G. E., & Barnhart, K. R. (2017). The SPACE 1.0 model: A Landlab component for 2-D calculation of sediment transport, bedrock erosion, and landscape evolution. *Geoscientific Model Development*, *10*, 4577–4604. https://doi.org/10.5194/gmd-10-4577-2017

Sieh, K. E. (1978). Slip along the San Andreas fault associated with the great 1857 earthquake. *Bulletin of the Seismological Society of America*, *68*, 1421–1448.

Sieh, K. E., & Jahns, R. H. (1984). Holocene activity of the San Andreas fault at Wallace Creek, California. *Geological Society of America Bulletin*, *95*(8), 883–896. https://doi.org/10.1130/0016-7606(1984)95<883:HAOTSA>2.0.CO;2

Stein, R. S. (1999). The role of stress transfer in earthquake occurrence. *Nature*, *402*(6762), 605–609. https://doi.org/10.1038/45144

Styron, R. (2019). The impact of earthquake cycle variability on neotectonic and paleoseismic slip rate estimates. *Solid Earth*, *10*(1), 15–25. https://doi.org/10.5194/se-10-15-2019

Sykes, L. R., & Menke, W. (2006). Repeat times of large earthquakes: Implications for earthquake mechanics and long-term prediction. *Bulletin of the Seismological Society of America*, *96*, 1569–1596. https://doi.org/10.1785/0120050083

Tarboton, D. G. (1997). A new method for the determination of flow directions and upslope areas in grid digital elevation models. *Water Resources Research*, *33*, 309–319. https://doi.org/10.1029/96WR03137

Trugman, D. T., Borsa, A. A., & Sandwell, D. T. (2014). Did stresses from the Cerro Prieto geothermal field influence the El Mayor-Cucapah rupture sequence? *Geophysical Research Letters*, *41*, 8767–8774. https://doi.org/10.1002/2014GL061959

Van der Walt, S., Schonberger, J. L., Nunez-Iglesias, J., Boulogne, F., Warner, J. D., Yager, N., et al. (2014). scikit-image: Image processing in Python. *Peer-Reviewed Journal*, *2*, e453. https://doi.org/10.7717/peerj.453

Walker, F., & Allen, M. B. (2012). Offset rivers, drainage spacing and the record of strike-slip faulting: The Kuh Banan. *Tectonophysics*, *530–531*, 251–263. https://doi.org/10.1016/j.tecto.2012.01.001

Wallace, R. E. (1968). Notes on stream channels offset by the San Andreas fault, southern Coast Ranges, California. In W. R. Dickinson, & A. Grantz (Eds.), *Proceedings of conference on geologic problems of San Andreas fault system*, *Publications*, (pp. 6–21). Stanford, California: Stanford University. https://doi.org/10.1017/CBO9781107415324.004

Wang, Y., Lin, Y.-N. N., Simons, M., & Tun, S. T. (2014). Shallow rupture of the 2011 Tarlay earthquake (Mw 6.8), eastern Myanmar. *Bulletin of the Seismological Society of America*, *104*, 261–284. https://doi.org/10.1785/0120120364

Wesnousky, S. G. (2005). Active faulting in the Walker Lane. *Tectonics*, *24*, 1–35. https://doi.org/10.1029/2004TC001645

Williams, R. T., Goodwin, L. B., Sharp, W. D., & Mozley, P. S. (2017). Reading a 400,000-year record of earthquake frequency for an intraplate fault. *Proceedings of the National Academy of Sciences*, *114*(19), 4893–4898. https://doi.org/10.1073/pnas.1617945114

Yadav, A., Bansal, B. K., & Pandey, A. P. (2016). Five decades of triggered earthquakes in Koyna-Warna Region, western India – A review. *Earth Science Reviews*, *162*, 433–450. https://doi.org/10.1016/j.earscirev.2016.09.013

Yuan, Z., Liu-Zeng, J., Wang, W., Weldon, R. J., Oskin, M. E., Shao, Y., et al. (2018). A 6000-year-long paleoseismologic record of earthquakes along the Xorkoli section of the Altyn Tagh fault, China. *Earth and Planetary Science Letters*, *497*, 193–203. https://doi.org/10.1016/j.epsl.2018.06.008

Zielke, O. (2018). Earthquake recurrence and the resolution potential of tectono-geomorphic records. *Bulletin of the Seismological Society of America*, *108*, 1399–1413. https://doi.org/10.1785/0120170241

Zielke, O., & Arrowsmith, J. R. (2012). LaDiCaoz and LiDARimager - MATLAB GUIs for LiDAR data handling and lateral displacement measurement. *Geosphere*, *8*, 206–221. https://doi.org/10.1130/GES00686.1

Zielke, O., Arrowsmith, J. R., Ludwig, L. G., & Akciz, S. O. (2012). High-resolution topography-derived offsets along the 1857 Fort Tejon earthquake rupture trace, San Andreas Fault. *Bulletin of the Seismological Society of America*, *102*, 1135–1154. https://doi.org/10.1785/0120110230

Zielke, O., Arrowsmith, R. J., Ludwig, L. G., & Akçiz, S. O. (2010). Slip in the 1857 and earlier large earthquakes along the Carrizo Plain, San Andreas Fault. *Science*, *327*(5969), 1119–1122. https://doi.org/10.1126/science.1182781

Zielke, O., Klinger, Y., & Arrowsmith, J. R. (2015). Fault slip and earthquake recurrence along strike-slip faults—Contributions of high-resolution geomorphic data. *Tectonophysics*, *638*, 43–62. https://doi.org/10.1016/j.tecto.2014.11.004